THE ASTROPHYSICAL JOURNAL, 390:514–535, 1992 May 10

THE SEPARATION BETWEEN GAS AND DUST FILAMENTS AT THE EDGE OF THE EXPANDING SHELL IN ERIDANUS

G. L. VERSCHUUR,[1] L. J RICKARD,[2] F. VERTER,[3] M. W. POUND,[4] AND D. LEISAWITZ[5]

Received 1990 October 3; accepted 1991 November 13

ABSTRACT

Adjacent filaments of ionized hydrogen, neutral hydrogen, and dust cross a 120 square degree region around $l = 187°$, $b = -50°$, at the boundary of a large expanding shell in Eridanus. The dust is visible on the *IRAS* Sky Flux Plates and looks like typical "interstellar cirrus." The morphology observed in H I emission is very similar, but with associated structures offset in position by amounts that vary across the region. The H I and IR filaments are $\sim 1°$ wide and are offset by up to 0.°8. All of the separation measurements have confidence levels of 95% or more. The H I and IR filaments are separated from parallel Hα filaments by 3°–4°.

For the H I and IR emission in this region of the sky, a point-by-point comparison yields a very weak correlation between I_{100} and $N_{\rm H\,I}$; however, when I_{100} at a dust feature is compared to $N_{\rm H\,I}$ at the associated (offset) H I feature, a relationship close to that reported by other workers is revealed. Specifically, the nature of the separation between gas and dust is that the primary H I filament is deficient in dust by an order of magnitude, whereas the corresponding dust filament has sufficient gas to reproduce the dust/gas mass ratio $\sim 1 \times 10^{-3}$ that is expected for cirrus.

Observations of CO emission from this region show that the separation between the structures in the H I and IR emission is not due to a transition of the gas into molecular hydrogen at the location of the IR filaments. Indeed, the molecular hydrogen column density of these filaments is at least two orders of magnitude below what is typically seen in high-latitude molecular clouds.

As the H I and dust in this region are associated with a large expanding shell (or superbubble), the action of shocks and radiation fields may be responsible for the separation of gas and dust. Such shells are believed to be common in the Galaxy, and therefore similar separations of gas and dust at other shell boundaries may be expected. Unless the gas and dust structures are resolved and lie in a favorable viewing geometry, the effect would tend to be hidden. Our results emphasize that it is not always evident, from observations with spatial resolutions coarser than a few arcminutes, how interstellar gas and dust are related.

Subject headings: dust, extinction — ISM: individual (Eridanus) — radio lines: atomic

1. INTRODUCTION

The H I distribution in an area of ~ 120 square degrees around $l = 187°$, $b = -50°$ (R.A. = 3^h4^m, Decl. = $-8°$) in Eridanus was fully mapped by Verschuur (1973; hereafter called Paper I) using the former 300 foot (91 m) telescope of the National Radio Astronomy Observatory.[6] He reported the presence of several dramatic H I filaments, narrowly defined in velocity, which were associated with an Hα filament found by Meaburn (1965, 1967). Sivan (1974) undertook a large-scale Hα survey and found that other filaments and related diffuse nebulosity existed in a region extending from $b = -55°$ to $b = +10°$ and $l = 180°$ to 230°. He suggested that all of this emission was associated with Barnard's Loop at 460 pc distance. Reynolds, Roesler, & Scherb (1974) also studied the diffuse galactic Hα emission and concluded that the same region was related to Gould's Belt which extends up to 300 pc from the Sun. Williamson et al. (1974) observed soft X-rays that trace the hot gas in the same general area; they found three extended regions of enhanced emission away from the Galactic disk, two of which lie on opposite sides of the filaments mapped in Paper I.

Heiles (1976), using larger scale, lower resolution maps, identified a 38° expanding shell of which the H I filaments discussed in Paper I are a part. He noted that the diffuse X-ray emission was strongest in the center of the H I ring, although the Williamson et al. data show a second strong X-ray source just outside the boundary of the H I ring. Reynolds & Ogden (1979) extended Heiles's discussion and suggested that the expanding shell is associated with the Orion OB1 association and Barnard's Loop. The H I filaments described in Paper I are at the southern edge of this shell and according to their model would be 400 pc from the Sun. However, they could not rule out that the filaments might be as close as 150 pc. The shell diameter in their model is 280 pc, which means that the filaments at $b = -50°$ are located several hundred parsecs away from the stars in the Ori OB1 association believed to be the cause of the ionization (Reynolds & Ogden 1979).

Figure 1 presents an overview of the 100 μm emission obtained from the Infrared Astronomical Satellite (*IRAS*) for the larger region encompassed by the Eridanus shell. These data were originally produced by Boulanger from the *IRAS* Zodiacal History File (see Boulanger & Pérault 1988) by empirical removal of foreground zodiacal emission. The location of prominent Hα and H I filaments identified in the above mentioned surveys have been schematically indicated. In

[1] 4802 Brookstone Terrace, Bowie, MD 20720.
[2] Mail Code 4213.3, Center for Advanced Space Sensing, Naval Research Laboratory, Washington, DC 20375.
[3] Mail Code 685, NASA Goddard Space Flight Center, Greenbelt, MD 20771.
[4] AT&T Bell Laboratories, Now at Astronomy Program, University of Maryland, College Park, MD 20742.
[5] NASA Goddard Space Flight Center, Now at Department of Astronomy, Pennsylvania State University, 525 Davey Lab, University Park, PA 16802.
[6] The NRAO is operated by Associated Universities, Inc., under contract with the National Science Foundation.

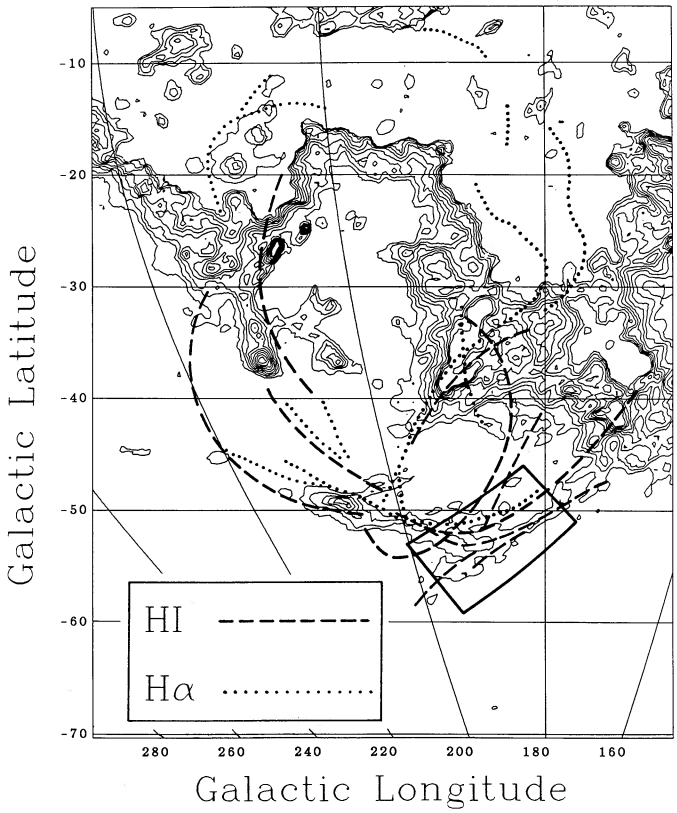

FIG. 1.—Large-scale map of the 100 μm infrared flux over the region of the expanding shell in Eridanus. Dotted lines indicate the approximate locations of Hα filaments recognized in the data of Meaburn (1965, 1967) and Sivan (1974). Since these data were not available in digital form it was not possible to do more than mark their position using graphed coordinate conversions. Noticeable is the large Hα filament which runs along the inside of the gas and dust filaments in the south. Dashed lines indicate the approximate location of filaments of H I identified in the 40′ resolution constant velocity maps of Colomb, Pöppel, & Heiles (1980). The Eridanus expanding shell has impinged "normal" gas here while the filaments at the southern boundaries indicate the high-latitude limits of the shell. The present paper considers the detailed structure of the filaments around $l = 187°$, $b = -50°$; the box marks the region displayed in Figs. 2–9.

general, the H I, IR, and Hα filaments are seen to define a shell-like structure. There is clearly an associated 100 μm structure, particularly around the southern rim. To the north, the low-latitude boundary of the 100 μm emission coincides with the boundary of the general H I distribution in this part of the sky, as can be seen in the maps of Colomb, Pöppel, & Heiles (1980). Several CO clouds (Magnani, Blitz, & Mundy 1985) are found to be coincident with a number of the filaments in Figure 1 and may owe their existence to physical processes occurring at the edge of the expanding shell.

In this paper we focus on the nature of the filamentary structure at the shell boundary around $l = 187°$, $b = -50°$, where the dust is related in an unexpected manner to both the H I filaments discussed in Paper I and the Hα filaments discussed by Meaburn (1965, 1967) and Sivan (1974). Section 2 discusses the data used in this study. Section 3 discusses the morphology of the various filaments, and in § 4 the physical parameters of the H I and dust structures are derived and compared. Section 5 considers why the various states of the gas and dust are separated and raises concerns about how cirrus and 21 cm data have been compared in previous studies.

2. H I, *IRAS*, AND Hα DATA

2.1. *Available* H I *Data*

Figure 2 shows 16 H I contour maps based on data taken with the NRAO 91 m telescope at velocities from +16 to −14 km s^{-1} (with respect to the local standard of rest [LSR]) in 2 km s^{-1} intervals, for the region centered at right ascension 3^h4^m, declination −5° ($\sim l = 87°$, $b = -50°$). These maps are from Paper I and refer to an area on the dust ridge at the southwestern edge of Figure 1. A map of the integrated column density of H I over all velocities (also taken from Paper I) is shown in Figure 3. The original data were obtained with a 10′ beamwidth and had to be smoothed to 20′ to make the maps because of limited data handling capacity available at the time. The channel separation was 1.43 km s^{-1} and the channel width after Hanning smoothing was 1.7 km s^{-1}. It was further broadened to 3.3 km s^{-1} before contour maps were made at 2 km s^{-1} intervals. The 150 K system temperature (Verschuur, Cram, & Giovanelli 1973) resulted in a 2.2 K peak-to-peak noise which was reduced by smoothing to 1.1 K. A beam efficiency of 0.64 was used to convert antenna temperature to brightness temperature (Verschuur, Cram, & Giovanelli 1973). The overall bandwidth coverage was 137 km s^{-1} centered at 0 km s^{-1}. No significant emission was found beyond the velocity limits in Figure 2 (also seen in the contour maps of Heiles & Habing 1974).

The right ascension scale in Figure 2 has been corrected for a 4 minute error apparently introduced in drafting the diagrams for Paper I. This was discovered from test profiles taken at the Bonn 100 m telescope (9′ beam), for which we thank T. Wilson. The Bonn observations were taken toward 18 positions that were supposed to be peaks in the H I emission of the NRAO 91 m map. When large discrepancies between the two data sets were found, an error in the coordinates of the NRAO 300 foot map was suspected. The magnitude of the error should only be an integral multiple of the tick marks on the original contour map, which were drawn at 4 minute intervals by computer but subsequently labeled by hand. The value of the error was then further constrained by taking a series of cuts across the filaments with the NRAO 140 foot (43 m) telescope (21′ beam), for which we are indebted to P. A. Henning and F. J. Kerr. The cuts were taken along declinations −02°11′, −03°15′, 04°00′, and −9°15′, with the observations spaced by 20′, for a total of 34 positions. These cuts located the ridges of the H I filaments, and their cross sections could then be used to measure the coordinate corrections. The data clearly confirm that the correction is 4 minutes in the center of the map, but at the northern end the H I profiles are less easily interpreted, owing to the discovery of substantial structure on scales of 10′ or less, which register somewhat differently in the different telescope beams. Finally, during a recent observing program at the NRAO 43 m, designed to detect magnetic fields in the direction of the filaments, one of us (G. L. V.) confirmed the correction by taking observations towards eight H I peaks and comparing them with NRAO 91 m observations of the peaks (see Table 1.) As a result of the many checking observations, and bearing in mind that we expect the coordinate correction to be an integral multiple of 4 minutes throughout the map, we are convinced that the map coordinates in Figure 2 are now correct. In the remainder of this section we summarize the checking observations and describe some of the small-scale structure in the region.

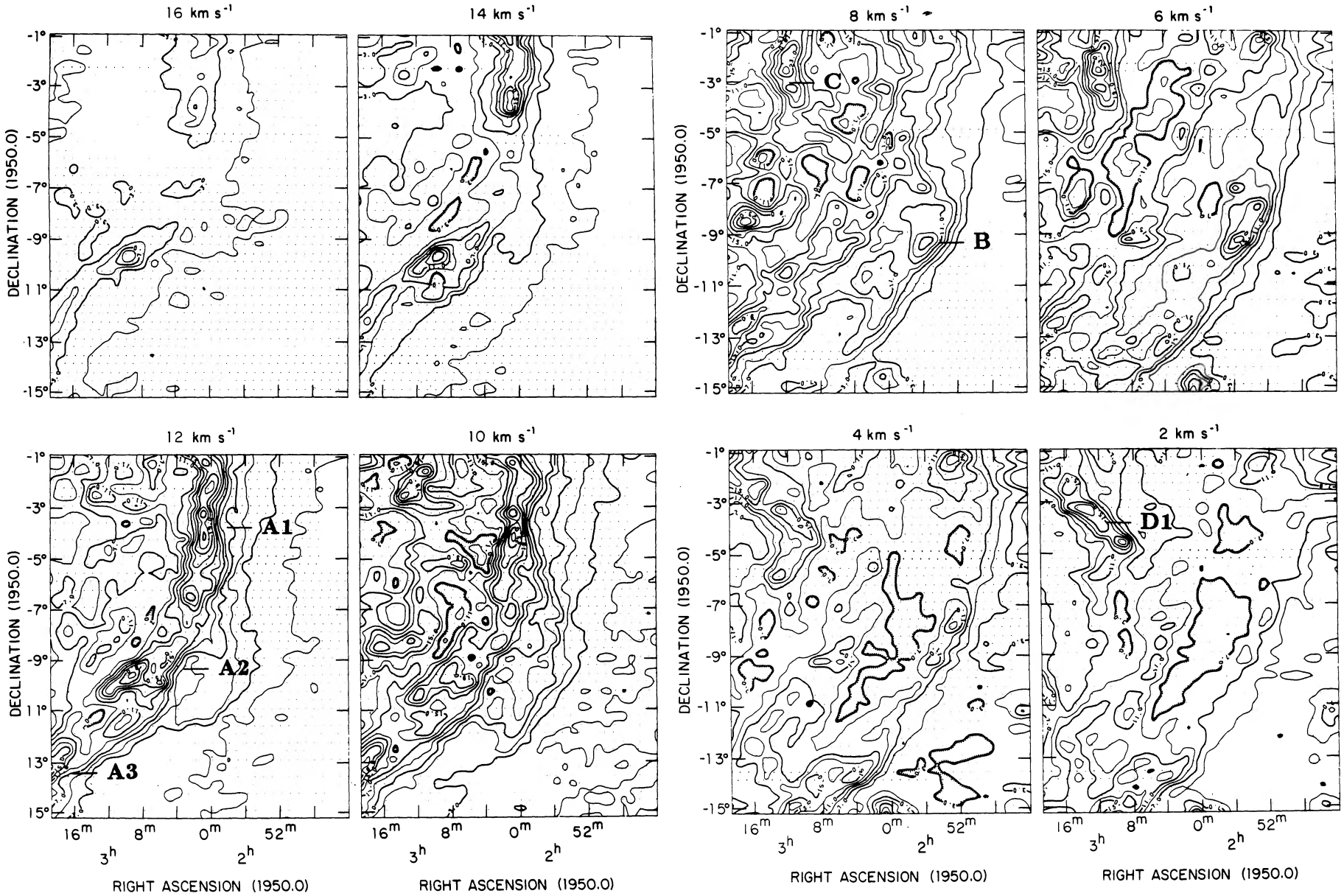

FIG. 2.—Channel maps of the NRAO 91 m 21-cm antenna temperature at constant velocities with respect to LSR taken from Paper I. Constant declination scans were spaced by 10′ and the data were smoothed to 20′ resolution to make these maps. Each dot indicates a data point used in the plotting program. At the upper right data were missing. The major filament A is clearly evident at $+12$ km s^{-1}. To the southwest of A, filament B is visible, especially at $+6$ km s^{-1}. At the upper left filament C follows a line of nearly constant right ascension in the maps at $+6$ and $+8$ km s^{-1}. Filament D is seen at $+2$ km s^{-1} and can be followed with changing velocity into the negative velocity maps. Antenna temperature contour are given for 1, 3, 5, 7, ..., K, with alternate contours indicated with heavier lines.

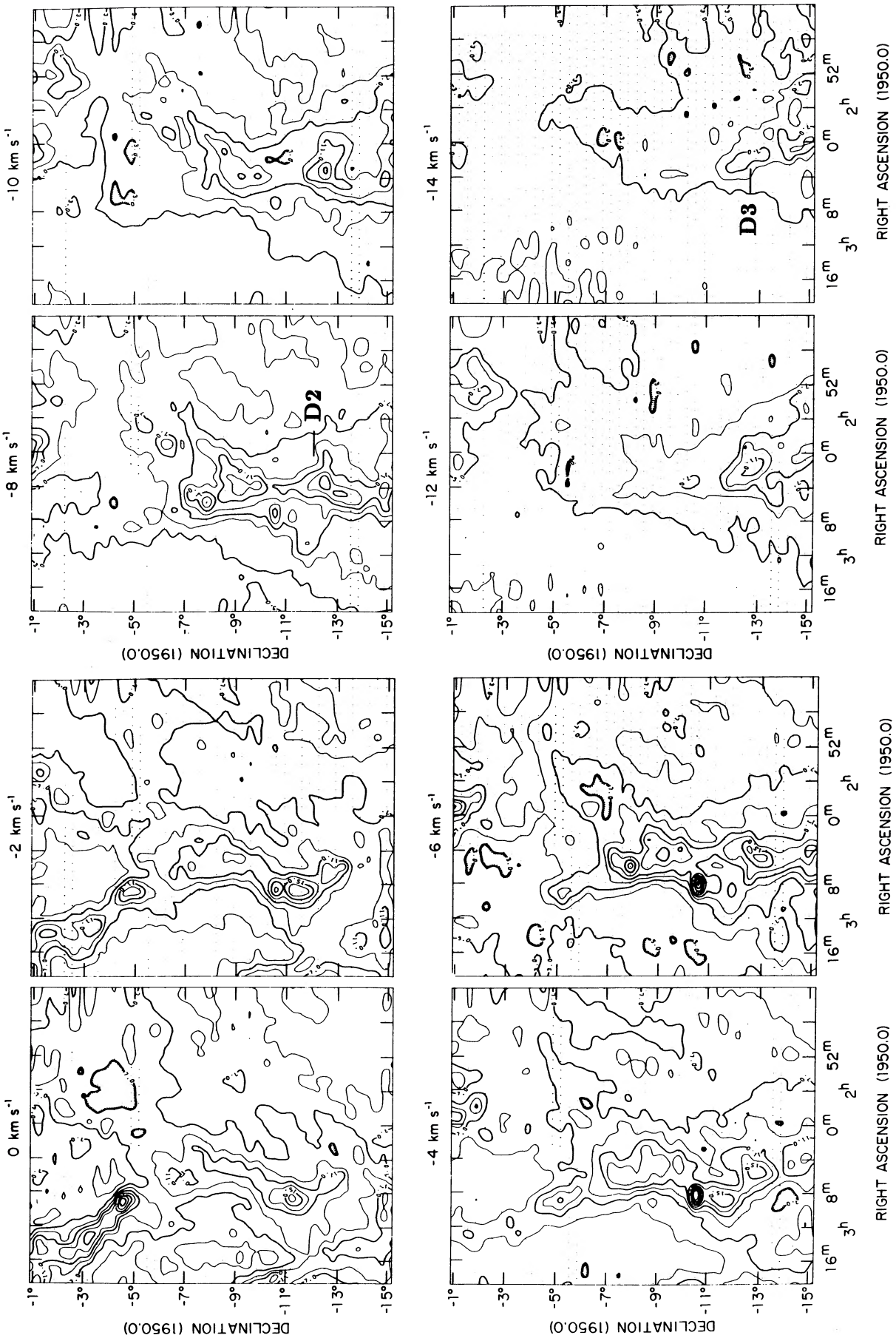

FIG. 2—*Continued*

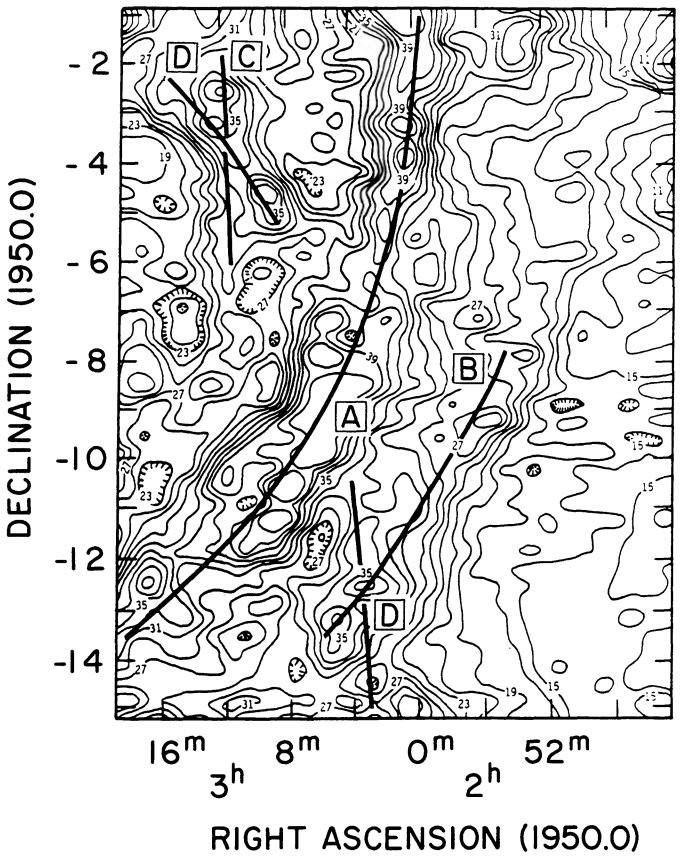

FIG. 3.—The column density of H I over the entire velocity range for the H I taken from Paper I. The contour interval is 2.1×10^{19} cm^{-2}. Filament A dominates the region although blending of features has reduced its contrast a little. Other filaments appear less prominent than on the individual velocity maps.

Because the only record of the 1973 91 m observations is the published contour maps, the check against the new observations was made by comparing the H I spectra in velocity steps that are provided by the channel maps in Figure 2. In order to illustrate the procedure, Table 1 lists the main features of NRAO 43 m and 91 m spectra toward H I peaks in the filaments. Subject to the limitations set by the contour interval (2 K) and channel interval (2 km s^{-1}) in Figure 2, there is generally good agreement.

Differences that arise between the original data and the checking observations by the 43 m seem to be due to small-scale structure in the H I distribution. For example, at one of the positions listed in Table 1 we also had a Bonn profile nearby, and this shows a reversal in the relative strengths of the two velocity components observed only 15′ away with the NRAO 43 m. In the smoothed 91 m map these two components are blended. In a case where we had two closely spaced Bonn profiles, components changed in brightness by a factor of 2; for example, the peak antenna temperature of a component at +5.4 km s^{-1} was 22 K (at $03^h09^m18^s$, −09°15′) while it was barely visible at 10 K in a direction 30′ away (at $03^h10^m12^s$, −09°35′). At the northern end of the map, point-to-point variations make it difficult to confirm positional correction in the Paper I data. For instance, along the cut of NRAO 43 m observations at declination −03°15′, the +10 km s^{-1} velocity component implies the right ascension correction is 5 minutes, whereas the +6 km s^{-1} velocity component implies it is 4 minutes.

When comparing H I observations from different telescopes, it is necessary to take account of differences in their antenna power patterns. The dominant effect influencing our work is the differing angular resolutions of the 91 m map (smoothed to 20′), the NRAO 43 m beam (21′), and the Bonn 100 m beam (9′). As would be expected from unresolved H I structure, many positions in the map register more strongly in the observations taken with a smaller beam. A second important effect is that stray radiation enters differently into the sidelobes of each tele-

TABLE 1

COMPARISON OF NRAO 43 METER AND NRAO 91 METER PROFILES

		140 FT DATA		300 FT DATA		
RIGHT ASCENSION (1)	DECLINATION (2)	Peak T_A (K) (3)	Velocity (km s^{-1}) (4)	Peak T_A (K) (5)	Velocity (km s^{-1}) (6)	COMMENTS (7)
$03^h01^m00^s$.....	−03°14′	17	+10.4	25	+10.0	Blend at peak (+7.5 km s^{-1})
03 01 00	−04 14	14	+8.5	25	+10.2	
03 08 00	−09 10	20	+5.6	19	+8.2	Double peak, blended in 91 m data
		22	+9.6	...	...	
(03 09 18	−09 15)	(23)	(+5.3)	...	...	(Bonn data 15′ away; T_A of peaks reversed with respect to above)
		(20)	(+10.6)			
03 09 10	−09 35	24	+9.1	20	+9.5	
03 11 00	−12 00	16.5	+7.7	15	+8.2	Double peaked
		12.8	−5.6	11	−3.0	
03 08 00	−10 36	19.0	+9.5	15	+10.0	Double peaked
		21.5	−5.9	21.5	−5.0	
03 10 24	−09 28	23	+11.2	14	+10.0	CO structure MBM15. Very complex profile
03 09 00	−04 34	16	+7.0	16	+8.0	Complex line, triple or more
		16	+1.9	19	+1.0	

COLS. (1) and (2).—Right ascension and declination of profiles obtained at the 43 m telescope; rms noise temperature 0.01 K.
COLS. (3) and (4).—The peak antenna temperature and velocity determined from the 43 m profiles. No Gaussian fitting was undertaken.
COLS. (5) and (6).—The peak antenna temperature and velocity determined from the 91 m contour maps in Fig. 2.
COL. (7).—Comments on the appearance of the various profiles.
The entry in parentheses gives data for a nearby profile obtained with the Bonn 100 m telescope.

scope. Lockman, Jahoda, & McCammon (1986) have made a careful study of this effect; they find that random noise and baseline error are comparable in H I surveys, but are both dominated by uncertainties from stray radiation. For the NRAO 91 m the typical 1 σ error in column densities was 1.0×10^{19} cm^{-2}, while for the NRAO 43 m it is 0.5×10^{19} cm^{-2} (Jahoda, Lockman, & McCammon 1990). For the purposes of checking our H I observations, we make two points about these possible discrepancies: First, it is extremely unlikely that differences in telescope resolution or sidelobe response could affect observations 50° below the Galactic plane so as to shift the centroid of the H I filaments and thereby invalidate either the coordinate correction or the separation from the IR filaments (especially considering that both effects occur over several resolution elements). Second, all of the H I and IR filaments that we will consider in this paper have column densities (either of measured H I or of implied H I for standard dust/gas ratios) that are at least 10 times greater than the quoted uncertainties, so there is no danger that the structures we describe are close to the noise or sidelobe levels and thus could be artifacts.

Despite the problems described above, there is a good average agreement between the channel maps and the checking observations, which were in the form of individual profiles. Over the velocity range of the major filament (+8 to +16 km s^{-1}, see below), the average H I column densities for 18 positions observed with the Bonn 100 m and the NRAO 91 m are 1.7 ± 1.0 and $1.9 \pm 0.8 \times 10^{20}$ cm^{-2}, respectively. Thus, on average the two data sets agree to within 1 σ.

The separations between gas and dust filaments that we claim in this paper are based on 21 cm and 100 μm maps that have been smoothed to a resolution of 20′. To first order, our conclusions should not be affected by unresolved small-scale structure (this is argued further in § 3.3). However, a complete high-resolution map of this region is desirable to elucidate the precise nature of the relationship between gas and dust in these filaments. The suggestion of substantial H I structure on scales of a few arcminutes is not seen in other diffuse filaments at high latitudes (e.g., Jahoda, Lockman, & McCammon 1990) and may be related to the mechanism that has caused the separation between gas and dust in Eridanus.

2.2. H I *Filaments at the Eridanus Shell Edge*

Figure 2 shows a filament of H I clearly evident at +10 and +12 km s^{-1} and we will refer to this as filament A. It shows three distinct segments, A1, A2, and A3, in the north, center, and south of the map. A faint, parallel structure, filament B, is seen to the southwest of A at +8, +6, and +4 km s^{-1}. At +8 and +6 km s^{-1} at the northern boundary of the map a small filament is found to the east of A and labeled C. Just south of filament C and inclined to it, another filament (D) is evident at +2 km s^{-1}. It has a clear velocity gradient along its length. With decreasing velocity it stretches toward the south and appears to bifurcate at low declinations; filament D curves at −2 and −4 km s^{-1}, and then straightens out at −8 km s^{-1}. At the southern edge of the maps at −12 and −14 km s^{-1} a second branch parallel to the ridge seen at −4 and −6 km s^{-1} is evident. Higher resolution data are needed to understand the detailed structure within all of these filaments.

In the map of H I column density (Fig. 3) filament A dominates while filament B is only weakly evident. Clearly, some of the structure at individual velocities has been lost against the background. To make meaningful comparisons with *IRAS* data, the morphology revealed in individual H I velocity maps is more important than structure seen in the integrated H I map. Indeed, identifying H I structure in this way is similar to identifying features of the IR data against a diffuse background, subtracting out the latter as a "baseplane." Note that in the subsequent discussions the same nomenclature will be used for associated IR and H I filaments.

In Paper I it was pointed out that the H I in this part of the sky exists as two distinct populations of "clouds." They were found to be concentrated at +8 and −8 km s^{-1} with respect to the LSR, not at 0 km s^{-1} as would be expected for undisturbed high-latitude gas in the anticenter direction. Analogous histograms of H I cloud velocities in two other fully mapped high-latitude regions showed a single-peaked distribution centered either at 0 km s^{-1}, or at a small velocity offset which could be attributed to galactic rotation (Verschuur 1974). The velocity of the H I in Figure 2 is therefore disturbed, with most of the matter either receding or approaching. If the filaments lie at the outer edge of the shell described by Reynolds & Ogden (1979), where only a small component of the expansion velocity should be in the radial direction, the ±8 km s^{-1} emission features correspond to a three-dimensional expansion speed greater than 8 km s^{-1}.

An unresolved bright 21 cm source can be seen in the −4 and −6 km s^{-1} maps in Figure 2 at 3^h08^m, −10°30′. This unusual feature was not mentioned in Paper I, because its narrowness in velocity and angle suggested that it could be radio interference. However, the profiles obtained for us by Henning & Kerr (private communication) using the 43 m telescope showed it to be real, a very bright H I structure unresolved in declination but slightly extended in right ascension. It appears to be associated with a small IR feature of similar orientation, and is a prime candidate for a closer look under high resolution.

2.3. *IR Filaments*

Figure 4 shows a 100 μm *IRAS* image of a region coincident with the H I maps. This image was produced by mosaicing Sky Flux Plates 98, 99, 122, and 123. Independent images were created from hours-confirmed sky coverages (HCON) 1 and 2. Background emission was removed from each image by fitting a tilted planar background to regions outside the bright filaments, and subtracting the model from the original images. Residual striping due to calibration differences among the individual *IRAS* detectors was removed by editing the Fourier transforms of the images. The two HCON images were then averaged together. Finally, the resultant image was reprojected to match the scale of the H I maps.

The presence of infrared filaments in Figure 4 is striking. Comparison with Figure 2 shows that each of the infrared filaments has a narrow velocity-width H I counterpart usually offset from it in angle. Figure 5 shows the 100 μm data convolved with a 20′ beam to enable direct comparison with the smoothed H I column density data in Figure 3. In view of our contention that positional offsets exist between H I and IR emission it is noted that *IRAS* Sky Flux Plates are free of significant positional errors (*IRAS* Catalogs and Atlases, Explanatory Supplement 1985; hereafter referred to as the *IRAS* Explanatory Supplement).

The prominent structure in the center of the map in Figure 4 contains several "bright spots" and, for convenience, we will refer to them as such. Their angular size is comparable with the resolution of the map (~4′), suggesting the presence of unre-

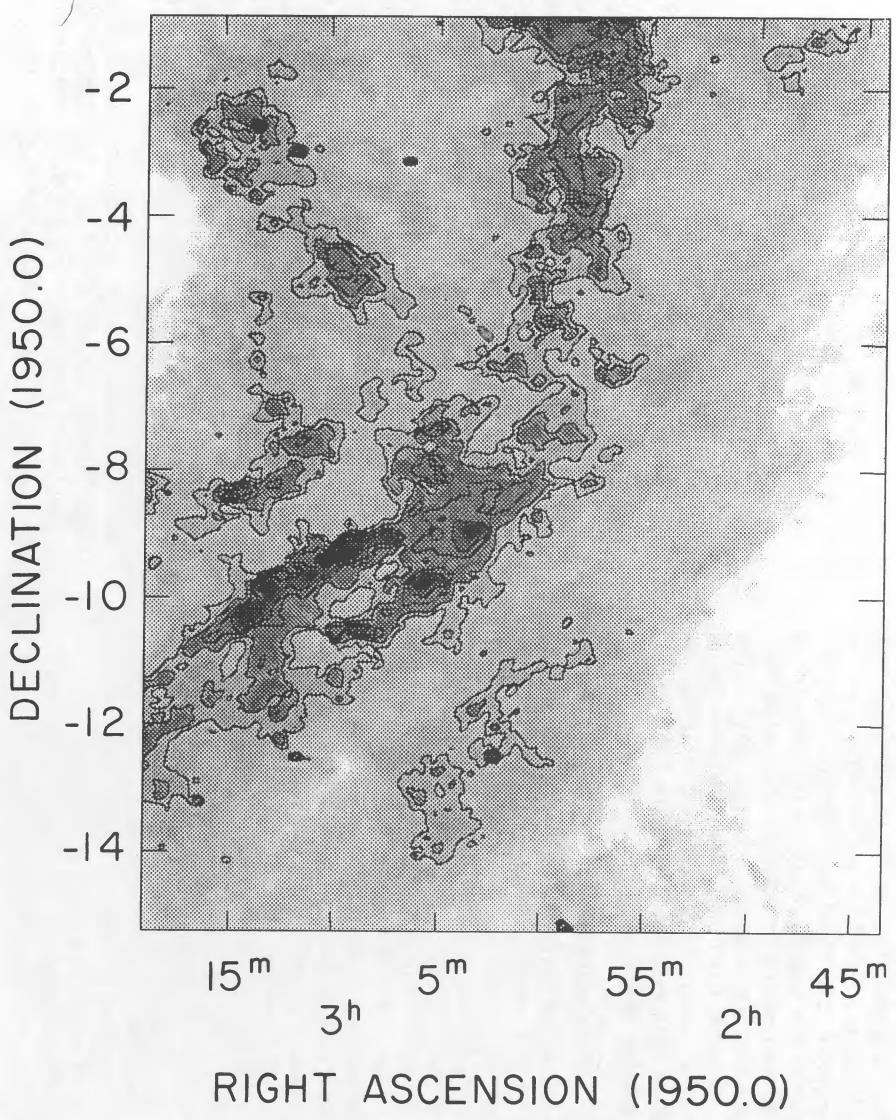

FIG. 4

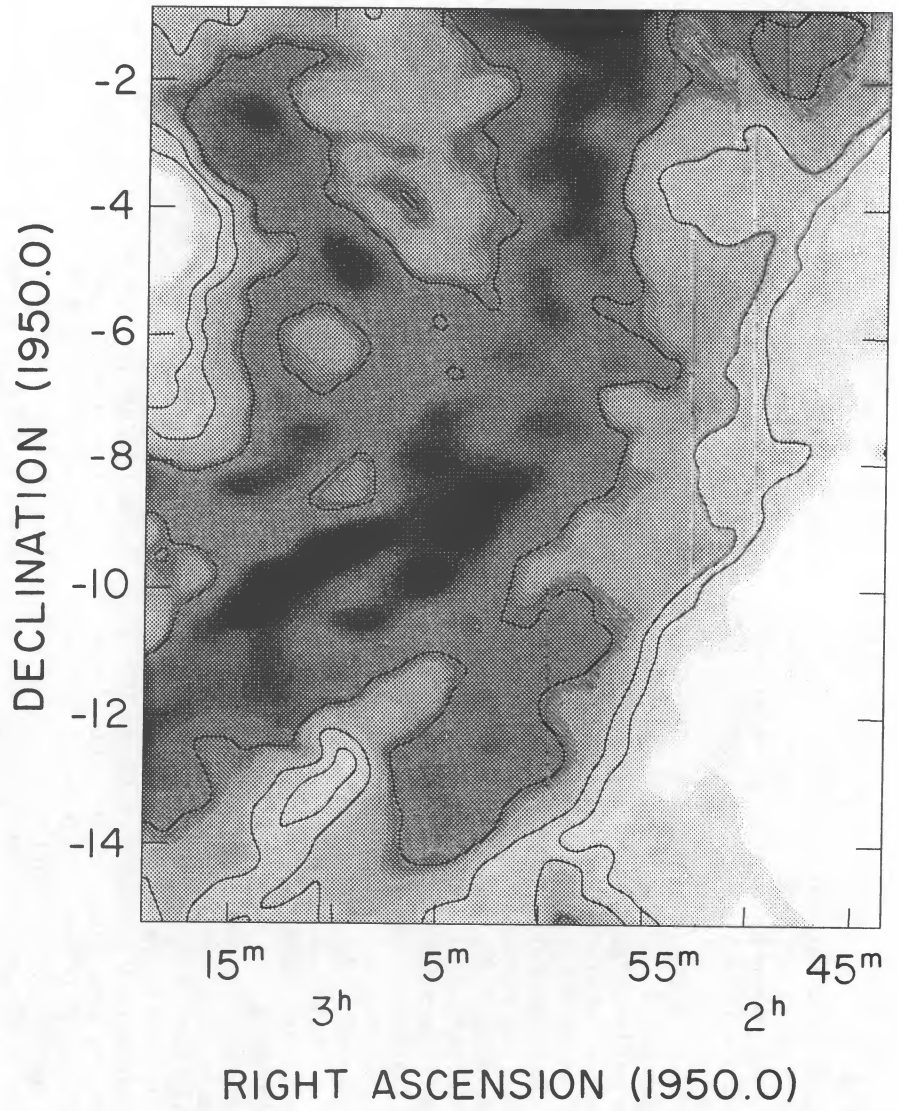

FIG. 5

FIG. 4.—The 100 μm destriped *IRAS* data for the region of Figs. 2 and 3. Contour levels are 2.4, 2.8, 3.4, and 4.0 MJy sr^{-1}. The cirrus equivalent of the major filament A is the prominent feature running from the top-center to the lower-left.

FIG. 5.—The 100 μm data convolved with a 20′ beam for the purpose of comparison with the 21 cm data of Figures 2 and 3. Contour levels are 2.4, 2.8, 3.4, and 4.0 MJy sr^{-1}.

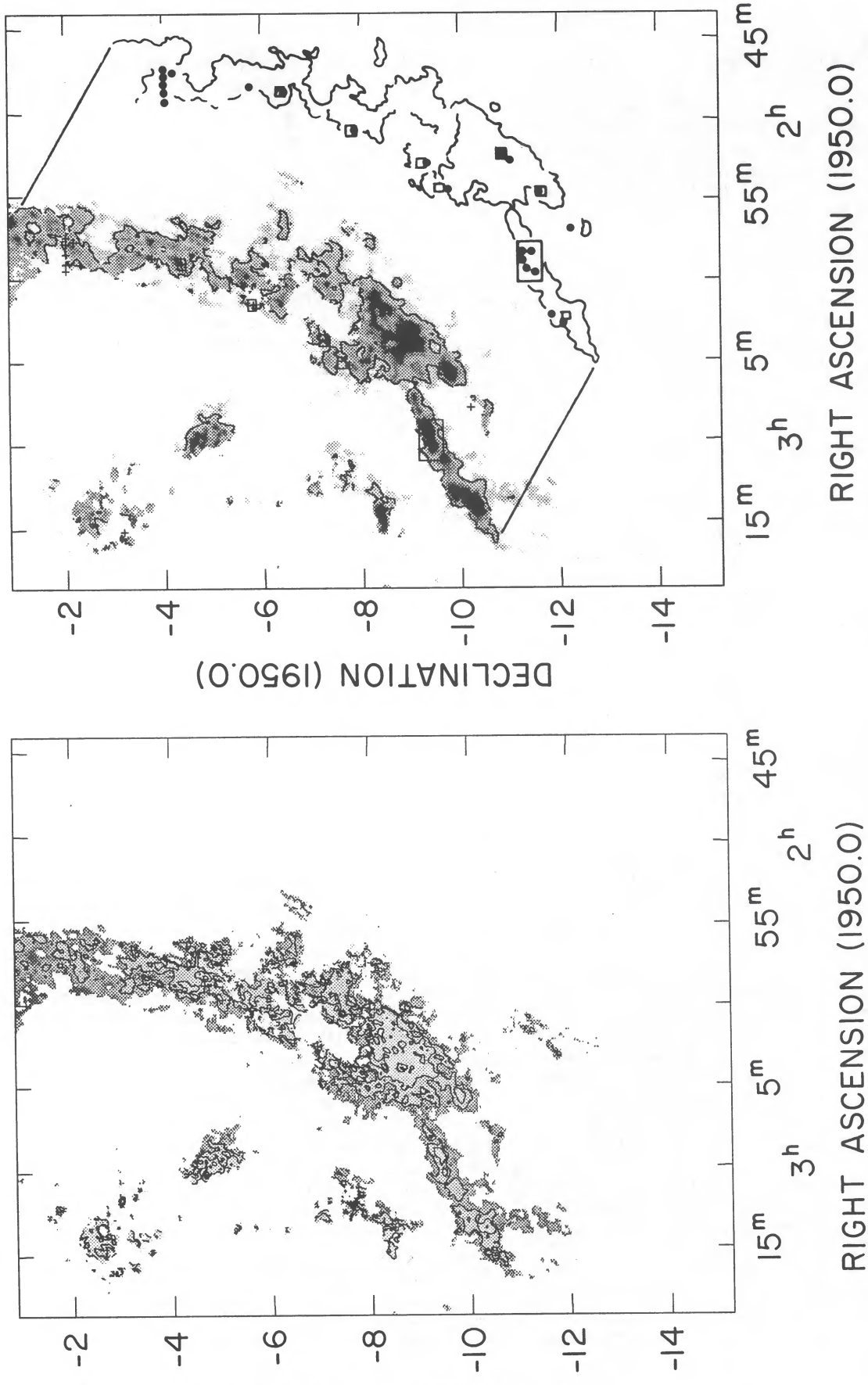

FIG. 6.—The map of the dust temperature obtained from the 100 and 60 μm *IRAS* data (see § 2.2). Contour levels are at 2 K intervals from 24 to 30 K. In the gray-scale representation, higher temperatures are darker.

FIG. 7.—Map of optical depth at 100 μm for the same region as previous figures, derived from the *IRAS* data (see § 2.2). In the gray-scale representation, higher opacities are darker. The dots indicate locations of CO observations made with the NRAO 12 m telescope and the various boxes indicate regions surveyed with the BL telescope (see text). The optical depth contours are at 4, 8, 12, 16, 20, and 24×10^{-6}. Because of the difficulty of seeing the dots and boxes on the gray-scale image, we have replicated the contour map (offset −9′.4 in R.A. and −1°.7 in Declination) above with CO observations marked by dots and boxes.

solved structure. Not presented here are the 60 μm data which show the same general morphology seen at 100 μm. Other than some very faint emission at 12 μm associated with the dust around 3^h9^m, $-9°15'$, no significant extended emission was detected at 12 or 25 μm. This finding is consistent with the Verter survey of infrared images of high-latitude molecular clouds associated with infrared cirrus; the 12 and 25 μm emission was detectable only in "bright spots" in the cirrus clouds (Verter, Magnani, & Dwek 1988).

Figure 6 displays the color temperature of the dust as determined from the 100 and 60 μm *IRAS* maps. Color temperatures were derived from the map in Figure 4 after additional background removal to isolate filament A, and a similarly processed map at 60 μm, by assuming thermal dust spectra with power-law emissivities [i.e., $I(\nu, T) = \nu^n B(\nu, T)$] convolved with the *IRAS* filter responses (*IRAS* Explanatory Supplement). We adopted an emissivity index $n = 1$; had we used an index $n = 2$, the derived temperature would have been 3–5 K cooler. (The difference is nonlinear, increasing strongly with T.) Two other sources of uncertainty in the color temperature are the background removal and the relative band-to-band calibration. Background removal is more critical for the 60 μm map, where an error of ~ 0.15 MJy sr^{-1} would have an effect comparable to the calibration error ($\sim 20\%$ in the 100 μm/60 μm ratio). Both errors are principally systematic, affecting mostly the absolute temperature level and not the appearance of Figure 6. Note that color temperatures are not displayed for all the pixels in Figure 4. Temperatures were not computed when the surface brightness in either band was less than the estimated 2 σ noise level (0.3 MJy sr^{-1} at 100 μm and 0.2 MJy sr^{-1} at 60 μm). In addition, temperatures are not displayed for those pixels for which the 2 σ error due to relative calibration uncertainty exceeded 8 K.

Figure 6 shows that the IR temperatures are generally ~ 30 K in the filaments. This is somewhat high for molecular cirrus but consistent with atomic cirrus. A typical dust temperature in molecular cirrus clouds is 23 K for an $n = 1$ grain emissivity (Verter, Magnani, & Dwek 1988), while the large-scale 100 μm/60 μm ratio of the galactic polar caps (see Table 4 of Boulanger & Pérault 1988) implies a dust temperature of 29 K. A closer examination reveals that the H I filament is slightly warmer than the IR filament. The difference is hard to see in the full-resolution map of Figure 6, but at 20′ resolution the mean IR temperature, ± 2 σ, for the centroids of the A1 filament (positions in Table 2, below) is 30.5 ± 0.9 K in the IR component and 36.9 ± 2.2 K in the H I component. No independent estimate of temperature in the H I clouds is available. Typical H I line widths, if interpreted as being due to thermal motions, correspond to a gas kinetic temperature, T_K, of ~ 250 K. More likely the lines are broadened by mass motion, possibly related to Alfvén waves within magnetically aligned filaments.

We also compute the IR optical depth at 100 μm from the ratio of the observed surface brightness to the modified Planck emission at the observed color temperature. The ratio is calculated at the appropriate effective wavelength for the convolution of the source spectrum with the *IRAS* filters. A map of the 100 μm optical depth is shown in Figure 7. The peak optical depth, $2.6(+2.4, -1.6) \times 10^{-5}$ (2 σ error bars), corresponds to an H I column density of 3.1×10^{20} cm^{-2} assuming reasonable dust properties (see § 4.2).

We have checked the computer programs used to generate our maps of *IRAS* dust temperature and opacity by comparing their results to the output of similar programs by E. Dwek and D. Clemens, for the same data. The programs agree to within 5%.

2.4. Hα *Filaments*

Figure 8 sketches the location of the Hα filaments derived from the mutually consistent data of Meaburn (1967), Sivan (1974), and Reynolds & Ogden (1979) and here they are located with respect to the IR optical depth data (Fig. 7) convolved with a 20′ beam. As was pointed out in Paper I, and also noted by Reynolds & Ogden (1979), the Hα and H I filaments are not spatially coincident. The separation between the Hα and parallel H I filaments is $\sim 3°$–$4°$. According to the Reynolds & Ogden (1979) model, the filaments exist at the boundary of what is, in essence, a low-density H II region created by a supernova that has swept the region clear of high-density material. The cavity appears to be a "superbubble" (Tenorio-Tagle & Bodenheimer 1988). Ionizing radiation from the Ori OB1 stars as well as some of the Gould's belt B stars (depending on the distance of the dust flaments) permeates the cavity and ionizes the inside edge of the H I filaments. As was noted in Paper I, the alignment of the optical polarization vectors with the filament axes suggests that magnetic fields are involved in the process determining the filamentary morphology.

3. MORPHOLOGY OF THE FILAMENTS

3.1. *On the Relation between* 21 cm, *IR, and* Hα *Emission*

The filamentary structures visible in the 21 cm line, the infrared, and Hα generally do not coincide. In Figure 9 (Plate 9), H I data from Figure 2 are shown superposed on the 100 μm *IRAS* data from Figure 4. Note the spatial alignment of the H I and IR filaments. The Hα in the region of our map resembles a "Y" (Fig. 8); two Hα filaments appear to cross at around R.A. 3^h15^m, Decl. $-7°$. The northeastern Hα segment parallels the H I filament A1 at $+10$ and $+12$ km s^{-1} (see Fig. 2*a*) and the northwestern Hα segment parallels the IR filament.

Next we discuss various emission features as if they were associated. These associations need not be physically meaningful for our main point to be true, which is that the gaseous filaments contain "too little" dust. Table 2 summarizes quantitatively the separation between adjacent H I and IR filaments that resemble each other. For each morphological segment, several cuts were taken across the filaments at the declinations listed in column (1). Along this cut, the right ascensions at which the H I and IR contour ridges peak are listed in columns (2) and (3), respectively. The H I peak was measured from the channel maps in Figure 2, and the IR peak was measured from the 100 μm brightness map convolved with a 20′ beam in Figure 5. Both peaks were determined by visual examination of the contour map data. An alternative way of defining the positions of the H I and IR filaments is to measure the center of their half-peak contours. These ridge centers are listed in columns (5) and (6) of Table 2. In some cases the ridge shapes made it difficult to measure the half-peak contours, or else there was no peak, so that these entries were left blank. For the ridge peaks and the ridge centers, the filament separations in degrees are listed in columns (4) and (7), respectively. Positive separations imply the H I filament is east of the IR filament. Obviously, due to the sinuous shapes of the filaments, there is a real variation in the separation between similar H I and IR features. For each of the morphological segments defined in

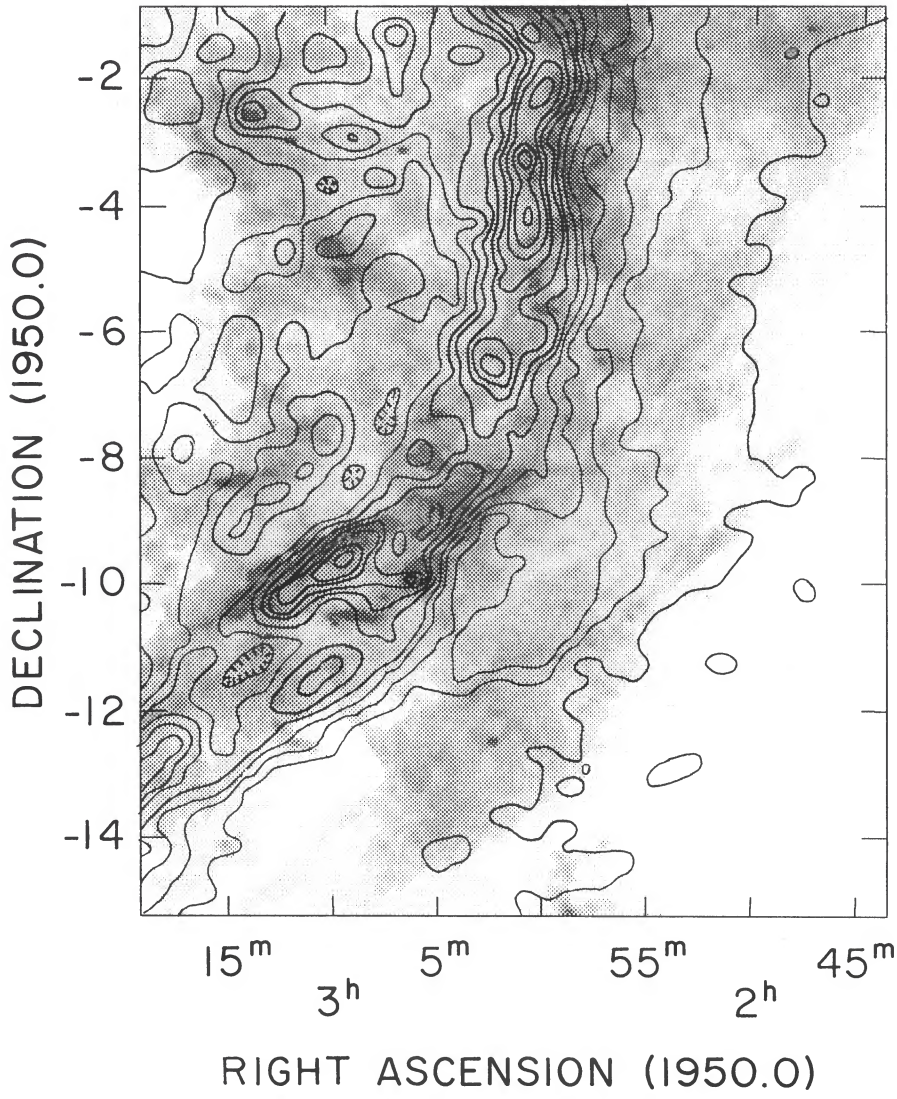

FIG. 9.—Overlay of the H I map at $+12$ km s^{-1} on the 100 μm data to show the offset between the gas and dust of filament A. At the top of the diagram the two filaments are well separated, and as they both curve to the east, they move slightly closer together, but at no place are their ridges perfectly coincident. The bifurcated structure in the center of the map can be seen in both the gas and dust distribution. The 100 μm image has been enhanced through pixel histogram equalization, to bring out the range of structures.

VERSCHUUR et al. (see 390, 522)

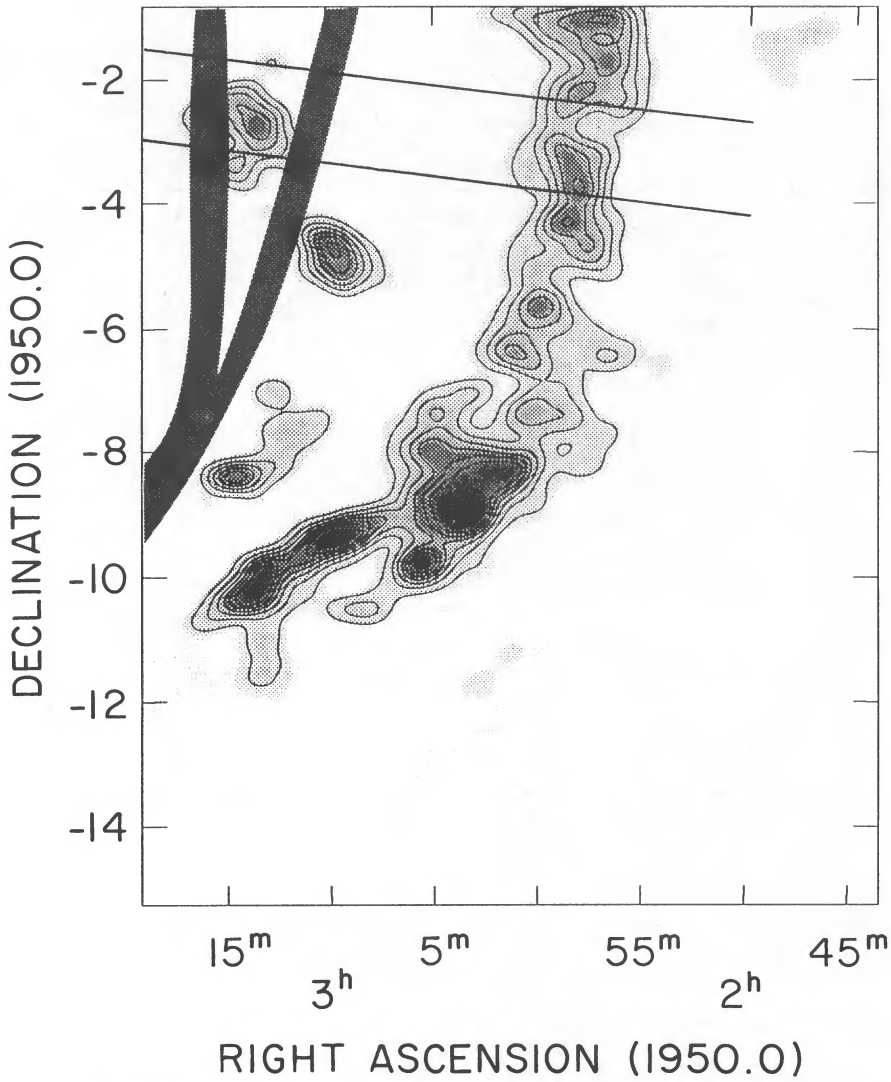

FIG. 8.—A sketch of the location of the ridge lines of the Hα filaments in the region (*hash marks*) taken from the references given in the text is here overlaid on the IR 100 μm optical depth convolved with a 20′ beam. The optical depth contours are at 1.2, 3, 4, 5, 6, 8, 10 × 10^{-6}. Note that the western arm of the Hα feature lies parallel to the IR filament while the eastern Hα arm is oriented parallel to the major H I feature at +10 and +12 km s^{-1} seen in Fig. 2 and also shown in the Fig. 9 overlay. Two straight lines indicate the cuts along which H I and 100 μm cross sections discussed in the text and shown in Fig. 13 were taken.

§ 2.2, the average separation and its 2 σ error bar (derived below) are given.

The measurement of the filament separation is essentially a test to see if two distributions (i.e., the filament cross sections) having different means (the filament positions) and variances (the uncertainties in the positions) can be distinguished from one another. In references on statistics, this is known as the Fisher-Behrens problem (Welch 1937; Mehta & Srinvasan 1970). We applied this theory to derive the 2 σ error bar on the mean separation between the H I and IR peaks of each filament segment in Table 2. The only assumption we have made is to take the variance of each mean to be 5′. This variance should characterize the possible errors in determining the peaks of the filaments and is much smaller than the filament widths, which are of order a degree. We feel that 5′, or roughly half a beam for the NRAO 91 m and Bonn 100 m H I observations, is a conservative estimate. Since the computed error bar is proportional to this variance, it can be linearly scaled to other assumed values. Comparing the mean filament separations and their uncertainties shows that all of the separations have confidence levels of 95% or more.

Examination of the overlay in Figure 9 shows that in the northwest corner of the map the main H I feature A is to the east of the IR filament. In the center of the map the two overlap in a complex region, and in the southeast corner they emerge apparently reversed with respect to each other. It is as if the two filaments twist around one another.

We have also used the available Hα data to estimate the average angular separation between the ionized hydrogen ridge and both the H I and the IR filaments. The northeastern segment of the Hα structure (Fig. 8) is parallel to and offset by 3°.5 from the H I filament A1 while the northwestern branch is parallel to and offset by 3°.1 from the corresponding IR filament A1. The separation between the Hα and the associated IR emission in filament A1 varies and is sometimes as large as 4°, or 7 d_{100} pc, where the distance of the filaments is given in units of 100 pc; d is believed to be ~400 pc (see § 4.1). If adjacent filaments are physically associated, the relative linear

TABLE 2

SEPARATION BETWEEN H I AND IR CIRRUS RIDGES

DECLINATION	RIDGE PEAKS			RIDGE CENTERS		
	R.A. IR	R.A. H I	Separation $\pm 2\sigma$	R.A. IR	R.A. H I	Separation $\pm 2\sigma$
Filament A1 (+12 km s^{-1})						
−1°0	2^{h}57^{m}2	3^{h}00^{m}5	0°83	2^{h}59^{m}0	3^{h}01^{m}5	0°63
−1.5	2 57.8	2 59.9	0.53	2 57.8	2 59.7	0.48
−2.0	2 57.4	2 59.5	0.53	2 57.2	3 00.0	0.70
−2.5[a]	2 56.0	3 00.5	0.75	2 57.8	3 00.5	0.68
	2 58.9	...	...	...	...	...
−3.0	2 59.3	3 00.8	0.38	2 59.2	3 00.8	0.40
−3.5	2 58.5	3 00.5	0.50	2 59.3	3 01.0	0.43
−4.0	2 58.3	3 00.6	0.58	2 58.7	3 00.8	0.53
−4.5	2 58.8	3 01.0	0.55	2 58.8	3 00.9	0.53
−5.0[a]	2 57.3	3 01.7	0.38	2 59.1	3 00.9	0.45
	3 00.2	...	...	...	...	...
−5.5	2 59.9	3 01.8	0.48	2 59.9	3 02.0	0.52
−6.0	3 00.0	3 02.0	0.50	3 00.3	3 01.7	0.35
−6.5[a]	2 56.7	3 02.3	0.35	2 59.4	...	...
	3 00.9	...	...	...	...	...
−7.0	2 59.1	3 01.5	0.60	2 59.3	3 00.5	0.30
−7.5	3 00.3	3 01.7	0.35	2 59.7	3 01.0	0.33
		Average	0.59 $\pm$0.07			0.49 $\pm$0.07
Filament A2 (West) (+10 km s^{-1})						
−8.5	3 03.6	3 04.0	0.10	3 03.4	...	...
−9.0	3 03.5	3 05.0	0.38	...	...	...
−9.5	3 05.1	3 05.8	0.18	3 04.8	...	...
−10.0	3 05.8	3 06.5	0.18	3 05.7	...	...
−10.5[a]	3 04.3	3 08.0	−0.10	...	...	...
	3 08.4	...	...	...	...	...
−11.0	3 08.8	3 08.4	−0.10	3 08.6	...	...
		Average	0.19 $\pm$0.11			
Filament A2 (East) (+12 km s^{-1})						
−8.5	...	3 05.0	...	...	...	...
−9.0	3 07.2	3 07.5	0.07	...	...	...
−9.5	3 10.1	3 09.4	−0.18	3 10.0	...	...
−10.0	3 12.9	3 10.9	−0.50	3 11.6	...	...
−10.5	3 14.1	3 12.6	−0.38	...	...	...
−11.0	3 13.2	...	...	3 13.2	...	...
−11.5	3 13.0	...	...	3 12.9	...	...
−12.0	3 12.6	...	...	3 12.8	...	...
−12.5[a]	3 12.2	...	...	3 13.2	...	...
	3 14.0	...	...	...	...	...
		Average	−0.25 $\pm$0.15			
Filament A3 (+12 km s^{-1})						
−11.0	3 16.3	3 15.0	−0.33	...	...	...
−11.5	3 16.0	3 15.7	−0.08	...	...	...
−12.0	3 17.8	3 16.3	−0.38	...	...	...
−12.5	...	3 17.0	...	...	...	...
−13.0	3 18.3	...	...	...	...	...
−13.5	3 18.1	...	...	...	...	...
−14.0	3 17.9	...	...	...	...	...
		Average	−0.26 $\pm$0.19			

TABLE 2—*Continued*

Declination	Ridge Peaks R.A. IR	Ridge Peaks R.A. H I	Ridge Peaks Separation ±2 σ	Ridge Centers R.A. IR	Ridge Centers R.A. H I	Ridge Centers Separation ±2 σ
Filament B (+6 km s^{-1})						
−10.0	2 58.5	2 57.5	−0.25	...	...	...
−10.5	2 58.8	3 00.5	0.43	...	...	...
−11.0	2 58.3	3 00.5	0.55	3 00.0	...	...
−11.5	3 02.1	3 03.0	0.23	3 01.5	...	...
−12.0	3 02.3	3 03.4	0.28	3 02.2	...	...
−12.5	3 02.2	3 03.4	0.30	3 02.9	...	...
−13.0	3 05.5	3 05.0	−0.13	3 03.3	...	...
−13.5	3 04.6	3 05.0	0.10	3 04.3	...	...
−14.0	3 04.9	3 05.5	0.15	3 05.0	...	...
		Average	0.18 ±0.09			
Filament C (0 km s^{-1})						
−1.0	3 10.5	...	...	3 10.9	...	...
−1.5	3 12.6	3 15.4	0.70	3 12.4	3 15.0	0.65
−2.0	3 13.4	3 15.0	0.40	3 13.8	3 14.8	0.25
−2.5	3 13.6	3 15.2	0.40	3 14.2	3 15.6	0.35
−3.0	3 13.1	3 14.5	0.35	3 13.4	3 14.0	0.15
−3.5	3 14.1	3 12.8	−0.33	3 12.9	3 12.8	−0.03
−4.0	3 11.6	3 11.2	−0.10	3 11.5	3 11.2	−0.07
−4.5	3 09.8	3 09.0	−0.20	3 09.7	3 10.8	0.28
−5.0	3 09.1	3 08.7	−0.10	3 09.1	3 10.1	0.25
		Average	0.14 ±0.09		Average	0.23 ±0.09
Filament C-A2 (+10 km s^{-1})						
−6.0	3 06.6	3 09.4	0.70	3 06.6	...	...
−6.5	3 06.0	3 07.9	0.48	3 06.6	...	...
−7.0[a]	3 03.7	...	...	3 04.0	...	...
	3 08.1	...	...	3 08.0	...	...
−7.5	3 05.0	3 07.3	0.58	3 05.0	...	...
−8.0	3 05.2	3 08.2	0.75	...	...	...
		Average	0.63 ±0.15			
Filament D (−6 km s^{-1})						
−6.0	3 13.4	3 11.7	−0.43	3 13.4	...	...
−6.5	3 13.3	3 11.7	−0.40	3 13.1	...	...
−7.0	3 12.6	3 11.6	−0.25	...	...	...
−7.5[a]	3 11.1	3 10.0	−0.28	3 11.2	...	...
	3 12.1	...	...	...	...	...
−8.0	3 12.1	3 11.0	−0.28	3 12.1	...	...
−8.5	3 14.3	3 13.0	−0.3	3 14.1	...	...
		Average	−0.35 ±0.11			

[a] There are two IR peaks; the separation is calculated with respect to the average of the two peaks.

displacement of gas and dust places an interesting constraint on the physical mechanism responsible for producing the filaments and determining their separation (see § 5).

The typical full width at half-maximum of the H I and IR filaments ranges from 0.°5 to 1.°2. The Hα filament widths as derived by us from the data of Meaburn (1965, 1967) and Sivan (1974), refer to a width of the large-scale features although fine structure is known to exist within these features (see § 3.3). In one Hα filament, where the data given by Reynolds & Ogden (1979) can be used to reconstruct a cross section, the feature is 1.°5 wide.

In the large-scale Eridanus shell displayed in Figure 1, there are varying degrees of anticoincidence between H I, IR, and Hα. Across the center of Figure 1 (crossing $l = 190$, $b = -37°$) a major filament is seen in both Hα and H I. The Hα runs along R.A. = 4^h (Reynolds & Ogden 1979). The H I is more prominent at the southern end of the Hα structure, and there are IR counterparts at the southern and northern ends, although in the north the infrared emission is less filamentary. The distribution is consistent with a viewing angle in which we are seeing the face of the expanding shell in that region (R.A. = 4^h, Decl = 0°; $l = 190°$, $b = -35°$).

The 21 cm maps of Colomb, Pöppel, & Heiles (1980) show that filament A extends as far as declination +10° ($l = 170°$, $b = -40°$) at approximately constant velocity (+12 km s^{-1}). Its length is 30°, which corresponds to 50 d_{100} pc. Whatever

forces are acting on the filament, they must accelerate it uniformly along a vast linear distance. Figure 1 also shows that an Hα counterpart to the 100 μm emission continues to be offset in angle over its full length. The weak H I filament B becomes very striking and straight south of declination −15°, the boundary of our maps, where it maintains a constant velocity. Weak dust emission is associated with it over a 10° length to the southern boundary of Figure 1.

3.2. *Association of* CO *with* H I *and* IR

One might suppose that the apparent deficit of atomic hydrogen in the peaks of the infrared filaments, evident upon inspection of Figure 9, could be explained by the presence of molecular hydrogen filaments that are coincident with the IR cirrus. In § 4.2 we will derive column densities for the H I and IR filaments, which quantitatively show that while the H I filaments are deficient in dust, the IR filaments do have sufficient atomic gas to reproduce the expected dust/gas ratio. Thus, on a point-by-point basis, there is no lack of gas in the dust filaments. However, the odd fact remains that at the locations of the IR structures there are no coincident structures in the H I map (e.g., see Fig. 13 below). Even if the morphological resemblance of the H I and IR filaments is not real or is not the product of a common origin, it is odd that the gas distribution does not contain peaks at the locations of the cirrus filaments. In this sense it is valid to speak of an apparent H I deficit in the IR filaments. The most natural explanation would be if the gas has undergone a phase transition and is predominantly molecular hydrogen in the cirrus filaments. To test this possibility, we searched for ^{12}CO, $J = 1$–0 emission, which is generally assumed to trace the presence of H_2. Magnani, Blitz, & Mundy (1985) have already detected CO emission at +4.4 km s^{-1} toward a single position (cataloged as cloud 15) located at $3^h10^m12^s$, −9°25′00″ (10′ north of the position published by them; L. Magnani, private communication).

Our initial search was conducted in 1989 January with the Harvard-Smithsonian Center for Astrophysics 1.2 m survey telescope. At 115 GHz, the telescope has a beamwidth of 8′.7. We searched 18 positions to an RMS noise of 0.15 K in T_A^*, using a velocity resolution of 0.65 km s^{-1} per channel. The only detection was at the corrected position of MBM 15.

A larger survey was carried out during 1989 February–April with a 1′.7 beamwidth of the AT&T Bell Laboratories (BL) 7 m telescope. The observations were made with 100 kHz filters, corresponding to a velocity resolution of 0.26 km s^{-1} at 115 GHz. A 38′ × 30′ region, including MBM 15, was mapped at 1′ spacing to an RMS noise level of typically 0.3 K. The region mapped is shown by the large box in Figure 7. The results are shown in Figure 10, which displays a contour map of integrated emission for the LSR velocity range 0–7 km s^{-1} superposed on gray-scale data for the 100 μm emission enlarged from Figure 4. (The CO contours have not been corrected for

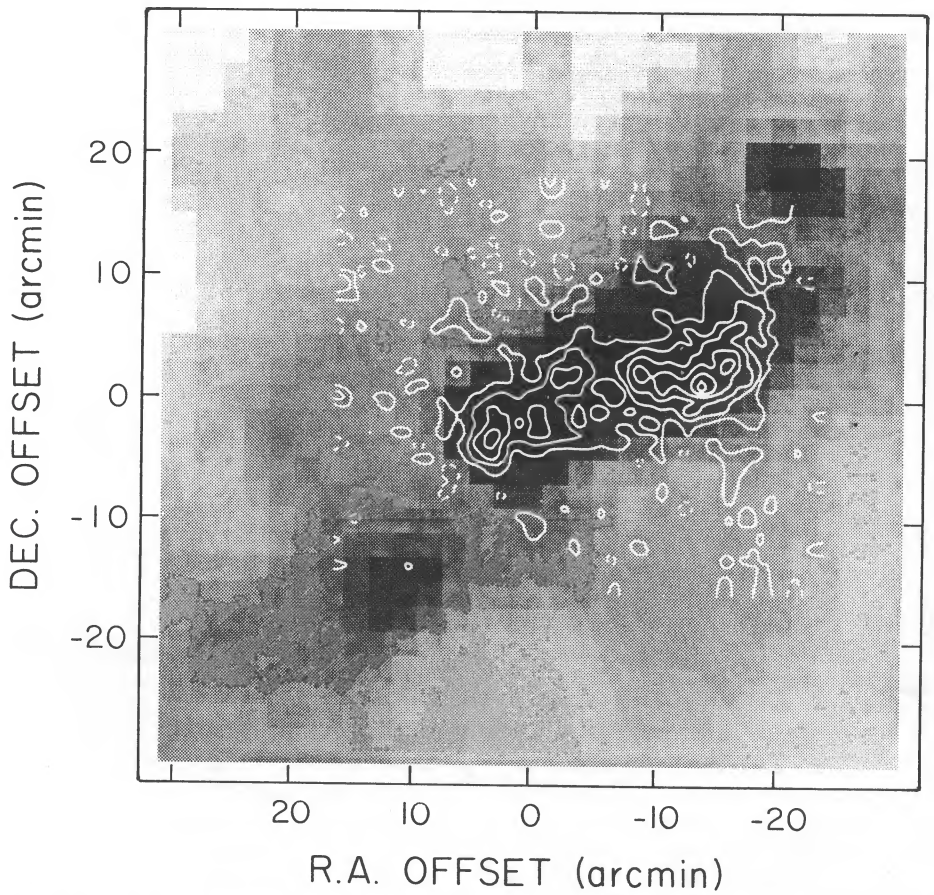

FIG. 10.—Integrated intensity of ^{12}CO $J = 1$–0, over the range from 0 to 7 km s^{-1}, as mapped by the BL 7 m telescope is overlaid on the contours of the 100 μm emission taken from Fig. 4. Map coordinates are given as offsets, in arcminutes, from $3^h10^m12^s$, −9°25′00″ (1950). The CO contours are 1.0 K km s^{-1} with a peak of 6 K km s^{-1}; the map values have not been corrected for the beam efficiency (0.9).

the beam efficiency of 0.9.) The map coordinates are offsets from the corrected position of MBM 15.

There is a CO complex extending ~25′ EW, with two main clumps each ~5′ in diameter. The eastern clump peaks at $3^h10^m24^s$, −9°23′30″, which is 0.2 and 3.5 S of the corrected position of MBM 15. The western clump peaks at $3^h09^m15^s$, −9°23′00″. Integrals over smaller velocity ranges are shown in Figure 11. They indicate that the two clumps each consist of several components and that all features are clustered around 4 km s^{-1}. Thus, the CO source resembles other molecular cores of infrared cirrus in both spatial and velocity structure (see Magnani, Blitz, & Mundy 1985). However, the CO structure is clearly offset from the local 100 μm emission peak. The eastern CO peak is 3′ SE of the IR peak; the western CO peak is at the edge of the IR structure, ~5′ S of the ridge of peak 100 μm emission. Furthermore, an H I emission peak at +12 km s^{-1} occurs 9′ south of the CO cloud (at declination −9°34′) while a weak H I feature at +4 and +6 km s^{-1} is found 19′ to the north, at declination −9°06′.

This region was also mapped with the BL telescope in ^{13}CO, with an RMS noise level typically 0.4 K; but no ^{13}CO emission was seen. Nine relative maxima within the map were searched for CS, $J = 2$–1 emission; their positions (in map coordinates) were (0′, 0′), (+3′, −4′), (+3′, −3′), (−3′, +2′), (−14′, +2′), (−17′, +2′), (−17′, +3′), (+1′, −2′), and (0′, −1′). The RMS noise levels were 0.06 to 0.08 K; but no CS emission was seen.

Additional 10′ × 10′ maps were made with the BL telescope around seven dust opacity peaks indicated by small boxes in Figure 7. The individual spectra have RMS noise levels of 0.25 to 0.35 K and show no emission.

We made another set of CO observations during 1989 June–July with the 12 m telescope of the National Radio Astronomy Observatory, at Kitt Peak. Taking advantage of the sensitivity of a new SIS receiver, we made fairly deep searches for CO emission toward 18 dust opacity peaks. In addition, we reobserved the two peaks in the BL integrated intensity map, and three other nearby positions. We also took fairly long integrations at a set of positions along declination −2°01′54″, running from the dust opacity peak at the western end to the local maximum in the H I emission at the eastern end. The positions observed are marked by dots on Figure 7 and the results are summarized in Table 3. Nearly all of the CO detections are in the vicinity of MBM 15. Of 23 positions more than 1° from MBM 15, there are only two secure and two tentative detections; all have temperatures (T_R^*) at ~10% of the level typical for high-latitude molecular clouds (see Magnani, Blitz, & Mundy 1985).

In order to evaluate our general failure to detect CO in the filaments, we determined the molecular column density in the detected regions. To do this, we searched with the NRAO 12 m telescope for ^{13}CO emission toward the two peaks of integrated intensity seen in the BL map near MBM 15. The results are given in Table 4. ^{13}CO emission was detected at each peak; the large ratio of ^{12}CO to ^{13}CO (>10) suggests that the ^{13}CO

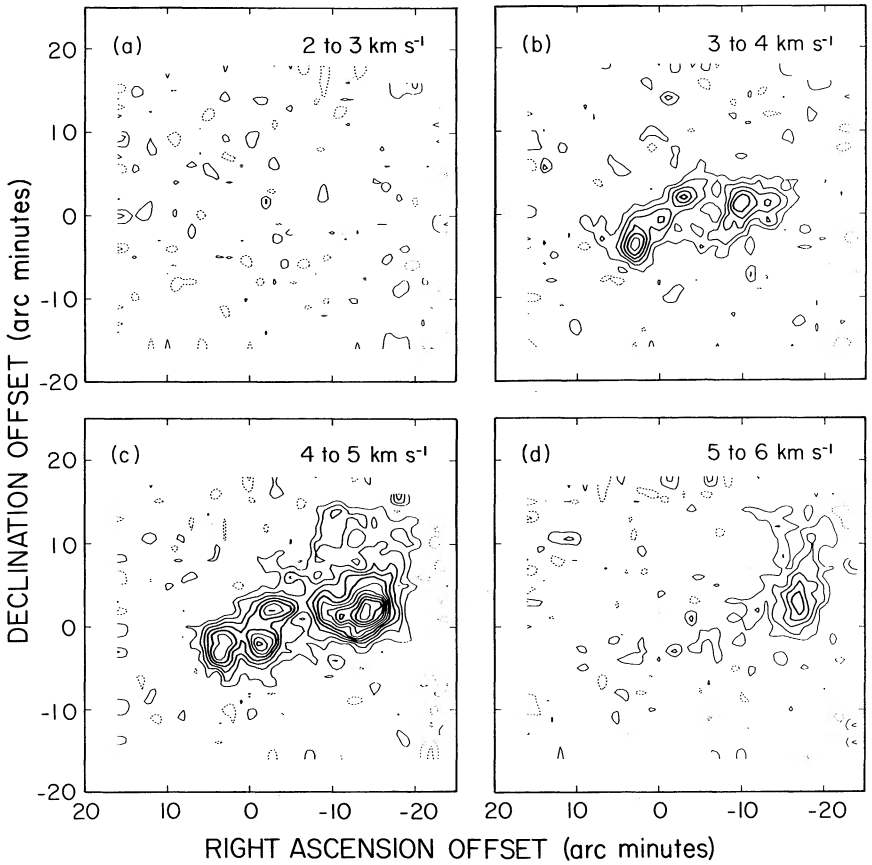

FIG. 11.—Channel maps of ^{12}CO $J = 1$–0 integrated intensity over 1 km s^{-1} ranges. The contours are 0.3 K km s^{-1}; otherwise, the map parameters are the same as for Fig. 10.

TABLE 3

NRAO 12 METER ^{12}CO OBSERVATIONS AT SELECTED POINTS[a]

R.A.	Decl.	Filter Width (kHz)	RMS Noise (K)	Integrated Intensity[b] (K km s^{-1})	Emission Centroid[c] (km s^{-1})
2^{h}57^{m}27^s.6	−2°01′54″	100	0.040	<0.062[d]	...
		30	0.136	<0.110	
2 57 51.6[e]	−2 01 54	100	0.062	<0.097	...
		30	0.193	<0.157	
2 58 27.6[e]	−2 01 54	100	0.049	<0.076	...
		30	0.136	<0.110	
2 59 03.6[e]	−2 01 54	100	0.063	<0.098	...
		30	0.207	<0.167	
2 59 27.6[e]	−2 01 54	100	0.059	<0.092	...
		30	0.180	<0.146	
2 57 43.2	−2 12 01	100	0.084	<0.131	...
		30	0.210	<0.170	
2 58 42.2	−3 46 35	100	0.048	<0.075	...
		30	0.129	<0.105	
2 59 02.0	−4 22 41	100	0.093	<0.145	...
		30	0.263	<0.213	
3 01 30.3	−5 50 00	100	0.057	<0.089	...
		30	0.152	<0.123	
3 03 09.0	−8 50 22	100	0.067	[0.193 (0.084)	10.22][g]
		30	0.176		
3 03 30.7	−8 59 09	30	0.186	0.477 (0.174)	10.94
3 03 41.4	−7 16 54	30	0.075	0.135 (0.062)	10.52
3 05 14.0	−7 45 24	100	0.058	<0.090	...
		30	0.156	<0.126	
3 05 27.2	−9 41 12	100	0.075	<0.117	...
		30	0.248	<0.201	
3 07 53.7	−10 13 33	100	0.134	<0.209	...
		30	0.331	<0.268	
3 09 10.0	−9 15 41	30	0.137	0.550 (0.100)	4.89
3 09 15.1[f]	−9 23 00	30	0.366	4.792 (0.292)	4.29
3 09 32.3	−9 16 38	30	0.154	0.553 (0.096)	4.50
3 10 11.1	−9 21 33	30	0.231	0.525 (0.166)	4.16
3 10 24.0[f]	−9 28 30	30	0.315	5.257 (0.226)	3.78
3 13 05.6	−9 48 14	30	0.124	[0.249 (0.122)	8.02][g]
		100	0.045		
3 13 35.8	−10 05 23	100	0.063	<0.098	...
		30	0.178	<0.144	
3 15 10.5	−3 09 21	100	0.046	<0.072	...
		30	0.129	<0.105	

[a] With some exceptions (noted below), these positions all correspond to peaks in the dust opacity at 100 μm.

[b] Integral of T_R^* over full line profile.

[c] Integral of $V_{LSR}\,T_R^*$ over full line profile.

[d] The upper limits to the integrated emission are 2 σ values, and assume lines of width of nine channels in the 100 kHz filters and 27 channels in the 30 kHz filters.

[e] Positions measured along a constant declination cut between a peak in the dust opacity and a peak in the H I emission.

[f] Peak in integrated emission in BL CO map.

[g] Tentative detection.

emission is optically thin. Combining our ^{13}CO results with the ^{13}CO/H_2 relation of Frerking, Langer, & Wilson (1982) for the Taurus Molecular Cloud envelope, we adopt the conversion $N_{H_2}/W(^{13}\mathrm{CO}) = 1.3 \times 10^{21}$ cm^{-2}/(K km s^{-1}). By using a main-beam efficiency $\eta_{M^*} = 0.86$, we find peak molecular column densities of 5.3×10^{20} cm^{-2}. If we assume physical conditions similar to the embedded MBM15 cloud, we may infer that the surrounding Eridanus filaments, having upper limits to the ^{12}CO integrated intensity typically 50 times lower than measured at the cloud peaks, have H_2 column densities typically less than 10^{19} cm^{-2}. By comparison, the average H_2 column density for high-latitude molecular clouds is 10^{21}cm^{-2} (Magnani, Blitz, & Wouterloot 1988).

To illustrate the relative amounts of observed gas and dust,

TABLE 4

NRAO 12 METER ^{13}CO OBSERVATIONS AT BL PEAKS[a]

R.A.	Decl.	Line	RMS Noise (K)	Integrated Intensity[b] (K km s^{-1})	Gaussian Fit T_R^* (K)	Gaussian Fit V_{LSR} (km s^{-1})	Gaussian Fit ΔV (km s^{-1})
3^{h}09^{m}15^s.1.....	−9°23′00″	^{12}CO	0.366	4.792 (0.292)	4.94	4.25	0.89
		^{13}CO	0.104	0.351 (0.082)	0.29	4.39	1.05
		^{12}CO/^{13}CO[c]	...	13.64 (3.30)	17.0	...	...
3 10 24.0.....	−9 28 30	^{12}CO	0.315	5.257 (0.226)	6.68	3.78	0.74
		^{13}CO	0.114	0.337 (0.082)	0.23	4.19	1.79
		^{12}CO/^{13}CO[c]	...	15.61 (3.84)	29.0	...	...

[a] All data given are for the 30 kHz resolution measurements.
[b] The integrated intensities, with 2 σ error.
[c] The ratio of the fitted peaks in T_R^*.

we have plotted the results for the five positions along declination −2°01′54″ in Figure 12. The offset betwen H I and IR features is ~30′ at this declination. The successive lines in the figure display the total H I column density, taken from Figure 3 in Paper I; the H I column density associated specifically with the feature at +12 km s^{-1} (averaged over 3.3 km s^{-1}), taken from Figure 2 in Paper I; the 100 μm opacity that has been converted to an equivalent gas column density (see § 4.2); and the limits to 2 × N_{H_2} inferred from the ^{12}CO upper limits. Clearly, the lack of H I structures at the locations of the IR filaments is not compensated by a rise in molecular hydrogen column densities.

Of course, the ^{12}CO emission might be low because of excitation effects. There is little difference in the dust temperature between the region near MBM 15 (29 K) and the filaments (28 K). But, it might be that the density in the filaments is too low for substantial collisional excitation of the $J = 1$ state. If we take the average width of the filaments (1°) in the IR map as a typical line-of-sight thickness, corresponding to 5 × 10^{18} d_{100} cm, then the condition $n(H_2) < 100$ cm^{-3} implies $N(H_2) < 5 \times 10^{20}$ d_{100} cm^{-2}. The observed H I column density over all velocities, typically 8 × 10^{20} cm^{-2}, would, at best, correspond to a density of 1.6 × 10^2 d_{100} cm^{-3}, and only marginally suffices to excite detectable CO emission. As will be shown in § 4.2, the H I associated with the filament velocity has an N_{HI} value of only 2 × 10^{20} cm^{-2} which would make the constraints even tighter.

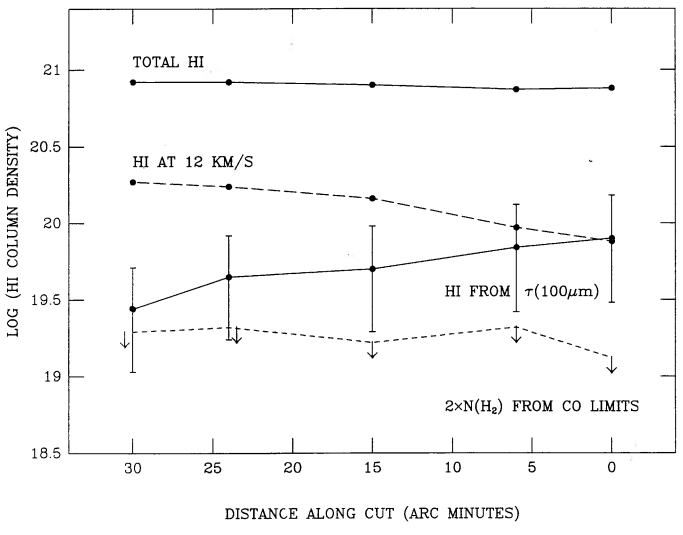

FIG. 12.—H I column densities of the filaments are plotted along a slice at declination −2°01′54″: (a) N(H I) over all velocities; (b) N(H I) for 12 km s^{-1} feature (averaged over 3.3 km s^{-1}); (c) N(H I) inferred from the 100 μm opacity, assuming a "normal" gas-to-dust ratio; (d) twice the $N(H_2)$ values inferred from the CO upper limits.

It is interesting to note that, at the few filament positions away from MBM 15 where CO is detected, the velocity corresponds roughly to that of the dominant H I component at that position. However, the clumps near MBM 15, which appear to be more like "normal" molecular cirrus, are at a velocity of 4.5 km s^{-1}, roughly midway between the velocities of the two major H I components at that position, 12 and −6 km s^{-1} (filaments A2 and D). One is tempted to say that a collision between the two H I features provides the density enhancement needed to make the CO near MBM 15 detectable.

Unless the CO emission in the vicinity of MBM 15 is induced by filament collision, an application of the de Vries, Heithausen, & Thaddeus (1987) procedure for deriving the conversion from CO emission to molecular hydrogen mass yields inconsistent results across our region. De Vries et al. (1987) assume that the I_{100} intensity is proportional to the gas density and that the background emission has been correctly removed, so that $I_{100} = aN_{HI} + bW(CO)$, and therefore $N_{H_2}/W(CO) = b/2a$. The constant a is computed by averaging data for positions with no detected CO. Using only the data for filament A (from the background-adjusted map isolating it), we have 13 upper limits (Table 3), yielding $\langle W(H\ I)\rangle_{no\ CO} = 96 \pm 16$ K km s^{-1} in the +12 km s^{-1} feature (assuming a velocity width of 3.3 km s^{-1}) and $\langle I_{100}\rangle_{no\ CO} = 1.97 \pm 0.35$ MJy sr^{-1}. (These errors are 95% confidence levels for the means, based only on the scatter in the measurements.) These imply $a = (1.22 \pm 0.27) \times 10^{-20}$ MJy sr^{-1} cm^2. If we use the data for Figure 4 (i.e., not isolating filament A) and the full H I profile, we derive $a = (0.45 \pm 0.06) \times 10^{-20}$ MJy sr^{-1} cm^2. Typical values are on the order of 10^{-20} MJy sr^{-1} cm^2 (see § 4.2).

The second step of the de Vries et al. procedure is to assume that a is the same for regions with CO and compute the constant b from the averaged data for our seven positions with definite CO detections: $\langle W(H\ I)\rangle_{CO} = 107 \pm 21$ K km s^{-1}, $\langle W(CO)\rangle = 1.76 \pm 0.78$ K km s^{-1}, and $\langle I_{100}\rangle_{CO} = 3.60 \pm 1.03$ MJy sr^{-1}, yielding $b = 0.80 \pm 0.78$ MJy sr^{-1} (K km s^{-1})$^{-1}$ and $N(H_2)/W(CO) = b/2a = (3.6 \pm 3.6) \times 10^{19}$ cm^{-2} (K km s^{-1})$^{-1}$. Thus, with 95% confidence, $N(H_2)/W(CO) < 0.7 \times 10^{20}$cm^{-2} (K km s^{-1})$^{-1}$, comparable to the values reported by de Vries et al. for the Polar Loop and by de Geus & Burton (1991) for the Ophiuchus complex, and quite low

compared to the value of 3×10^{20} typical of the high-latitude molecular clouds (Magnani et al. 1988) and of dark clouds (Bloemen et al. 1986).

This leads to the perplexing situation that the filaments are CO-rich near MBM 15, and molecule-poor farther away. However, if the filaments without detectable CO emission are not deficient in molecules but just underexcited, we will have underestimated a, and more normal values of $N(H_2)/W(CO)$ are allowed.

3.3. *Small-Scale Structure in the Filaments*

It is likely that the gas and dust in this region are clumped on smaller scales than our observations can register. It is conceivable, although contrived, that variations in this clumping and hence its beam dilution could produce the apparent separation of gas and dust.

The smallest infrared structures in these filaments are unresolved. On the *IRAS* Sky Flux Plates the 100 μm emission is structured on scales ranging from several degrees to the resolution limit of the plates ($\sim 4'$). It has been noted by Bazell & Desert (1988) that infrared cirrus in general is well fitted by a fractal structure. Thus, in principle, clumpiness of the dust (and probably the gas) distribution may persist to smaller scales than we have been able to resolve. Small-scale clumpiness is also suggested by the fact that the extinction data at 8′ resolution (Magnani & de Vries 1986) do not show the embedded, dense clumps in high-latitude molecular clouds that are inferred from observations of the molecular gas at 1′ resolution (Turner, Rickard, & Xu 1989).

The smallest atomic and ionized gas structures in the filaments are unresolved. Structures on the order of a few arcminutes are unresolved in the new 21 cm data discussed in § 2.1. Recent VLBI observations by Diamond et al. (1989) have shown that structure in the atomic interstellar medium exists on a scale of 25 AU, although such structure is considered rare at high Galactic latitudes (Jahoda, Lockman, & McCammon 1990). Sandage (1976) has shown that at least one of the Hα filaments in this region contains structure down to arcminutes in size.

The existence of very small molecular structures may explain the apparent lack of hydrogen in the dust filaments. Our millimeter observations show small, probably resolved, molecular clumps. It is known that some IR cirrus clouds have molecular cores (Magnani, Blitz, & Mundy 1985) that are highly clumped on spatial scales as small as 6500 AU (Pound, Bania, & Wilson 1990) and velocity scales as small as 0.35 km s^{-1} (Magnani et al. 1990). However, the hypothesis of variable molecular clumping is a dubious explanation for the results in Table 3. It is too much of a coincidence that CO observations pointed at the highest peaks of dust opacity find low upper limits. In those molecular cirrus clouds that have been well studied, the IR peaks have dense molecular clouds associated with them (Turner et al. 1989).

4. SOME PHYSICAL PARAMETERS FOR THE REGION

4.1. *Distance to the Filaments*

A lower limit of 30 pc is set by the proper motion upper limits in the Hα filaments by Elliot & Meaburn (1970). Reynolds & Ogden (1979) subsequently argued that the expanding shell—of which our filaments are a part—is associated with the Orion OB1 association at a distance of 460 pc. They sketched the morphology of the region and placed our filaments at the southern edge, ~ 400 pc from the Sun. However, R. J. Reynolds (private communication) does not rule out that these structures could be as close as 150 pc as suggested by Heiles (1976). Reynolds & Ogden (1979) did not take into consideration optical polarization data for stars at known distances seen toward the filaments. As was reported in Paper I (also see Korhonen & Reiz 1986), several stars as nearby as 100–150 pc have polarization vectors parallel to the axes of adjacent or positionally coincident filaments. If the filament orientation is indicative of the magnetic field direction, the polarization observations suggest either that the dust is closer than 100 pc or the magnetic field causing the polarization is ordered over a depth of several 100 pc. Pending more definitive data, we will use the 400 pc distance estimate and continue to indicate how derived parameters vary with distance.

4.2. *Predicted and Observed Gas/Dust Ratio*

There is no direct one-to-one positional correspondence between the IR and H I peaks, although the brightest 100 μm emission usually is found next to a feature in the atomic gas. A dramatic example is the IR ridge in the center of the mapped area around 3^h10^m, $-9°30'$. It lies alongside the unresolved edge of a bright H I feature visible in both the $+12$ km s^{-1} map, Figure 2, and in the integrated H I map, Figure 3.

Dust opacity data (Fig. 7) were used to predict the amount of dust in the H I filaments for comparison with their observed atomic gas content. The observed 100 μm optical depth is roughly related to the column density, N_{HI} by $\tau_{100} = \mu\, m_H\, N_{HI}\, \kappa_d\, Z_d$, where μ = mean molecular weight of the atomic gas ($= 1.26$), m_H = mass of a hydrogen atom, Z_d = relative abundance (by mass) of grains, and κ_d is the mass absorption coefficient of the grains. We take $\kappa_d = 41\ (100\ \mu m/\lambda)^n$ cm^2 g^{-1}, $n = 1$, and $Z_d = 9.5 \times 10^{-4}$ for outer galaxy cirrus (Sodroski et al. 1987). We note that the IR-radio determination of dust/gas mass ratio $Z_d \sim 1 \times 10^{-3}$ (Sodroski et al. 1987), is markedly lower than the traditionally accepted optical-UV determination $Z_d \sim 1 \times 10^{-2}$ (Bohlin, Savage, & Drake 1978). However, any increase in Z_d will only strengthen our results proportionately. Thus, our adopted dust-to-gas conversion is $(\tau_{100}/10^{-6}) = 8.2\,(N_{HI}/10^{20}\ \mathrm{cm}^{-2})$.

Two cross sections normal to filament A1 (see Fig. 8) were examined to compare H I and dust. To make quantitative comparisons with the available 21 cm data, we used the IR optical depth data that were convolved with a 20′ Gaussian beam and converted to equivalent N_{HI} values using the above relationship. Figure 13 shows the two sets of profiles. The H I associated with filament A covers the $+12$ to $+8$ km s^{-1} velocity range, and we used the map of the H I density integrated over an 8 km s^{-1} velocity width (defined and given in Paper I) to determine the variation of N_{HI} due to this filament alone. Figure 13 illustrates both the clear offset between the gas and dust ridges in filament A1 (average separation 0.°6; Table 2), as well as the drastic variation in the dust/gas ratio as one proceeds along a slice perpendicular to the filaments.

Table 5 provides a quantitative comparison of the observed versus inferred H I column densities for a series of positions in filament A1 that correspond to the H I and IR ridge centers along the declination slices that were listed in Table 2. For either the H I to IR filament, we compare the observed N_{HI} at the filament center of the N_{HI} inferred from τ_{IR} via the adopted dust-to-gas conversion. Both N_{HI} and τ_{IR} are measured as differences of the filament above the local background emission. The observed N_{HI} is taken from the channel map at $+12$ km

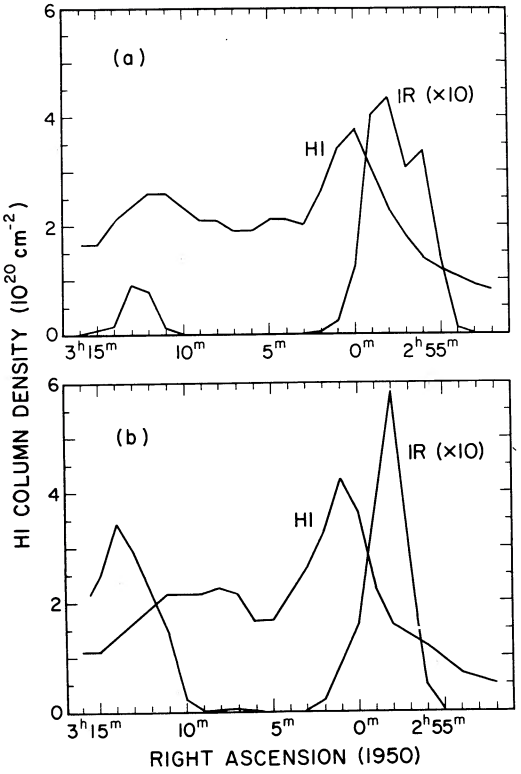

FIG. 13.—Comparison of H I and dust content in filament A1 along two cross sections shown in Fig. 8. The 100 μm optical depth map of Fig. 8 that was convolved with a 20′ Gaussian beam was used to make the comparison and the derived optical depths were converted to equivalent H I column density using the relationship given in the text. The data derived from the IR opacity are scaled by a factor of 10 for display. The H I data refer to those taken from Paper I over the velocity range corresponding to that filament only. (*a*) A cross section running through 3^h20^m, $-1°.52$ and 2^h50^m, $-2°.7$. (*b*) A cross section running through 3^h20^m, $-3°.0$ and 2^h50^m, $-4°.25$.

s^{-1} in Figure 2. For the IR filament, these slices indicate that the average inferred N_{HI} is $(0.54 \pm 0.06) \times 10^{20}$ cm^{-2}, while the average observed N_{HI} is $(0.64 \pm 0.15) \times 10^{20}$ cm^{-2}. Thus, the gas and dust contents of the IR filament are consistent, to within 2 σ, with the adopted dust/gas ratio. However, for the H I filament, the average inferred N_{HI} is $(0.18 \pm 0.06) \times 10^{20}$ cm^{-2}, whereas the average observed N_{HI} is $(1.26 \pm 0.13) \times 10^{20}$ cm^{-2}. There is an average excess column density of $(1.08 \pm 0.14) \times 10^{20}$ cm^{-2} of atomic gas in the H I filaments. This is not a very large column density, but it is an order of magnitude greater than the gas content which would be expected from the dust/gas mass ratio. Moreover, this is a lower limit on the dust deficiency, because we have used only a narrow velocity range for the observed N_{HI} (only 2 km s^{-1}, versus an integral over 8 km s^{-1} in Fig. 13) and have adopted a lower limit to the dust/gas mass ratio.

The properties of filament A1 that are presented in Table 5 are characteristic of the region. The only way for the dust/gas ratio to have the nominal value in the H I filaments is for approximately 90% of the dust in those structures to be hidden. Given the preferential sensitivity of *IRAS* to warm dust, this could be done by invoking a large population of cold dust, or by imagining that the dust temperature is higher in the IR filament. However, we have already noted in § 2.3 that the IR temperature is, in fact, slightly higher in the H I filament, on the inner edge of the shell. The "missing" dust equivalent to 10^{20} cm^{-20} of gas could be concealed in the H I filament only if its temperature is below19 K. Unless vast quantities of dusty gas are hidden in clumps within the filaments, it is difficult to imagine how cold dust could persist in this diffuse rim of a shell created by an energetic event.

4.3. *Correlation between Gas and Dust in the Region*

Many authors have discussed the correlation of I_{100} with N_{HI} and for the sake of making direct comparisons we present some estimates of I_{100}/N_{HI} in the filaments as well as over the area covered in our study.

Boulanger & Pérault (1988) have used the *IRAS* Zodiacal History File to derive I_{100}/N_{HI} for the solar neighborhood at high Galactic latitudes. They found the ratio to be constant to within a factor of ~ 3 in bins of 0°.5 over scales of 100 pc, with a value of 0.85×10^{-20} MJy sr^{-1} cm^2 at the polar caps. Variation in the ratio from region to region can be attributed to variation in the interstellar radiation field. Similarly, Deul (1988) found $I_{100}/N_{HI} = 1.07 \times 10^{-20}$ MJy sr^{-1} cm^2 from a decomposition of infrared emission in the Galactic plane. He also studied eight cirrus clouds and found the ratio to vary between 0.9 and 3.0×10^{-20} MJy sr^{-1} cm^2, again probably due to heating variations. Heiles, Reach, & Koo (1988) measured 1.3×10^{-20} MJy sr^{-1} cm^2 in atomic clouds, while de Vries et al. (1987) estimated 1.0×10^{-20} MJy sr^{-1} cm^2 in a high-latitude region north of the Galactic plane. These values are in agreement with the value of 1.0×10^{-20} MJy sr^{-1} cm^2 expected theoretically (Draine & Anderson 1985). Our data, however, suggest very different values. A point-to-point comparison between I_{100} and N_{HI} over our region (from Figs. 3 and 4) is shown in Figure 14. Data spaced 2^m in right ascension and 1° in declination at 104 positions produced a relationship $I_{100}/N_{HI} = 0.15\,(\pm 0.06) \times 10^{-20}$ MJy sr^{-1} cm^2. The relationship is only marginally significant (the correlation coefficient $r = 0.43$, with 99% confidence limits on this coefficient ranging from 0.24 to 0.59), a conclusion at odds with the results of the other workers discussed above. If we look only at the data at positions of H I or IR peaks, the correlation does not improve significantly.

In the discussion in § 3.1 it was noted that virtually every peak and valley in the H I filaments has a similar, usually offset, partner in the IR data. This suggested that the H I and IR structures are true physical counterparts. We identified 28

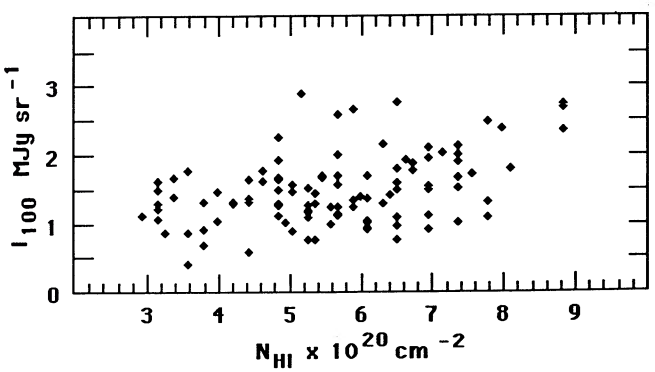

FIG. 14.—Direct point-to-point comparison of observed I_{100} with N_{HI} using 104 data points located in a uniform grid in right ascension and declination. Scatter in the diagram and lack of any clearly defined dependence between these two parameters contrasts strongly with an apparent relationship found by others in similar studies.

TABLE 5

COMPARISON OF H I AND DUST COMPONENTS IN FILAMENT A1

DECL.	R.A.	$S(60\ \mu m)$ (M Jy sr^{-1})	$S(100\ \mu m)$ (M Jy sr^{-1})	T (K)	N_{HI} Inferred (10^{19} cm^{-2})	N_{HI} Observed (10^{19} cm^{-2})
			IR Component			
−1°0	2^{h}59^{m}0	0.73	1.94	32.3	5.23	8.5
−1.5	2 57.8	0.68	1.96	31.3	6.11	3.8
−2.0	2 57.2	0.55	1.69	30.4	6.03	2.8
−2.5	2 57.8	0.47	1.36	31.3	4.22	4.7
−3.0	2 59.2	0.65	1.80	31.7	5.31	5.7
−3.5	2 59.3	0.60	1.58	32.4	4.20	5.7
−4.0	2 58.7	0.54	1.64	30.6	5.69	4.7
−4.5	2 58.8	0.39	1.42	28.6	6.89	6.6
−5.0	2 59.1	0.31	1.01	29.8	4.01	9.4
−5.5	2 59.9	0.39	1.36	29.1	6.08	8.5
−6.0	3 00.3	0.26	1.04	27.8	5.83	10.4
Averages:				30.5	5.42	6.4
$\pm 2\sigma$				±0.9	±0.58	±1.5
			H I Component			
−1.0	3 01.5	0.62	1.30	35.7	2.26	10.4
−1.5	2 59.7	0.70	1.47	35.6	2.57	11.3
−2.0	3 00.0	0.64	0.99	40.7	1.02	14.2
−2.5	3 00.5	0.60	0.89	41.4	8.65	13.2
−3.0	3 00.8	0.67	1.17	38.7	1.46	12.3
−3.5	3 01.0	0.66	1.27	36.9	1.91	15.1
−4.0	3 00.8	0.41	0.65	40.3	6.95	16.0
−4.5	3 00.9	043	0.88	36.1	1.44	14.2
−5.0	3 00.9	0.42	1.11	32.6	2.88	12.3
−5.5	3 02.0	0.27	0.48	38.4	6.20	9.4
−6.0	3 01.7	0.26	0.86	29.6	3.52	10.4
Averages:				36.9	1.75	12.6
$\pm 2\sigma$				±2.2	±0.60	±1.3

pairs of peaks and 11 pairs of minima in the two maps (Figs. 3 and 5) and measured their positions. In some cases where an elongated IR peak consisted of two components, the unsmoothed IR data in Figure 4 were used to determine the locations. If the offset infrared and neutral hydrogen feature pairs correspond to gas and dust that initially occupied the same volume, then one might expect the 100 μm intensity in an infrared peak to "match" the column density in the "associated" atomic gas feature in a ratio consistent with the average values reported elsewhere. Indeed, we found this to be the case. The average relationship measured between I_{100} and N_{HI} in the pairs of associated peaks and valleys taking into account all the H I gas in those directions (not just the difference of the filament above background), is given by $I_{100}/N_{HI} = 0.55\ (\pm 0.10) \times 10^{-20}$ MJy sr^{-1} cm^2 (correlation coefficient 0.86). It may be more appropriate to include only the 21 cm emission at the filament velocity because of the clear relationship between IR and H I filaments. (H I at other velocities is probably quite unrelated and contributes only to an offset in the derived column densities). In this case we obtain $I_{100}/N_{HI} = 0.31\ (\pm 0.78) \times 10^{-20}$ MJy sr^{-1} cm^2 (correlation coefficient 0.22).

If the gas-dust offsets and the relationships between I_{100} and N_{HI} seen in Eridanus are common, then many studies of the large-scale correlations between H I and IR emission (e.g., Boulanger & Pérault 1988) obtained with low-resolution H I data may in fact be averaging over physically separated matter. (Verschuur 1992 will discuss this in the context of other regions observed with high resolution.)

5. DISCUSSION

5.1. *Why Do the* H I *and* IR *Filaments Not Coincide?*

We suggest that the noncoincidence of gas and dust filaments in this region resulted from shock and radiation processing of the interstellar medium during the history of the creation of the Eridanus superbubble. Interstellar material that has been swept up by multiple stellar winds and supernovae may have incomplete collisional coupling between particles of dust and gas, or may suffer grain destruction (see the review by Seab 1987). Unfortunately, even the best models of these effects are sensitive to large uncertainties in the detailed behavior of grains (e.g., McKee et al. 1987) and have not been run in conditions which simulate the Eridanus filaments. In this section, we briefly review the basic physics of the processes which may be involved.

The filaments in our region of study show very strong evidence of having been shocked. In Figure 9 it is easily seen that the main filament describes a clearly defined arc which extends continuously over 12°. At a source distance of 400 pc, this corresponds to a physical length of 84 pc. It is hard to imagine how such a long interstellar filament could form, unless it is part of a shell swept up by a pressure front. Whether this shell is driven by radiation, stellar winds, or supernovae, it is liable to have an initial velocity in excess of the sound speed in the interstellar medium, and hence the filament has been shocked. In addition to the suggestive appearance of the filaments, the velocity structure of H I in the filaments shows that each morphological segment is moving at a narrowly defined velocity,

and these velocities follow a progression across the filaments (see Fig. 2). This velocity signature argues strongly that the morphological segments really are coherent entities and that their movement has been propelled.

Additional arguments that these filaments have been shocked comes from their association with the Eridanus shell, the most striking example of a large expanding H I shell in the high-latitude sky (Heiles 1976). The full structure, of which our filament A is a part, maintains a nearly constant velocity (+10 to +12 km s^{-1}) over 30°. The energy necessary to create the Eridanus shell, $3.8 \times 10^{50}\ d_{150}$ ergs (150 pc is a minimum distance) calls for a supernova, possibly into a pre-ionized cavity (Heiles 1976). The shell is currently expanding at 23 km s^{-1} (Heiles 1976). If the shell is assumed to be in the "snowplow" phase of hydrodynamic supernova models, then the age of the remnant is $1.7 \times 10^6\ d_{400}$ years (400 pc is the distance we adopt in § 4.1).

The radiative precursor to a supernova explosion may have helped to separate the gas and dust in the Eridanus filaments. Radiation couples more strongly to dust than to gas. Could the dust have streamed radially outward under this pressure, creating the observed offset, with the dust rim outside of the gas? Gilman (1972) has shown that, under the conditions relevant to circumstellar envelopes, the momentum absorbed by grains from the radiation field is efficiently transmitted to the surrounding gas and drives stellar mass loss. To our knowledge, this effect has not been modeled under conditions relevant to interstellar cirrus in supershells.

A second process which causes dust exposed to a radiation field to begin to stream radially outward through the gas is the "rocket effect," discussed by Reddish (1971). Grains adsorb gas isotropically, but desorb anisotropically because they evaporate molecules preferentially from the irradiated side of the grain. Brand & Zealey (1975) have shown that dust exposed to the standard interstellar radiation field can acquire a relative drift velocity of 2 km s^{-1} in ~6000 yr. However, their estimate ignores the spiralling of charged dust grains around interstellar magnetic field lines, which is the dominant drag mechanism in modern dust evolution models, and might extinguish the rocket effect.

The arrival of a shock front causes a combination of grain acceleration and destruction. Due to the charges on their surfaces, dust grains spiral around the magnetic field lines parallel to the shock front. As the shock cools, the magnetic field increases along with the gas density, and the grains attempt to conserve their magnetic moment by spinning up. This "betatron acceleration" (Spitzer 1976) leads to a streaming of dust through gas, which in turn leads to dust destruction by nonthermal sputtering and grain-grain collisions (Seab 1987). Grains of intermediate size (≈0.05–0.25 μm) suffer the most destruction; smaller grains are stopped almost immediately, and larger grains are not appreciably accelerated. Seab & Shull (1983) show that the velocities and destruction rates of grains in a shock peak just before the recombination plateau.

The observed separation of gas and dust filaments at the edge of the Eridanus shell, and in particular the severe dust deficiency in the H I filament, might be explained by destroying the grains on the inner edge of the shell. The trouble with this scenario is that the region is not currently undergoing a radiative shock fast enough ($v \sim 100$ km s^{-1}) to significantly destroy grains, and postulating a past event does not explain why the grains were not destroyed throughout, instead of leaving an apparently normal IR filament adjacent to the dust-deficient H I filament (C. G. Seab, private communication). One is led to a two-stage scenario, in which the dust-depleted H I filament later plows into the normal IR filament. But this does not explain why the two filaments bear such an extreme morphological resemblance to each other, as though they were once coincident.

Clearly, a complete explanation of the phenomenon seen in Figure 9 must await a detailed theoretical treatment, although the complex morphology of this region suggests that several effects are acting at once. Also, a higher resolution (beamwidth < 10′) H I survey of the region is needed to clarify the detailed structure of the filaments.

5.2. *Is Anticoincidence between Gas and Dust Common?*

Offset between H I and IR structures appears present, albeit less dramatically, in maps of other regions as well. For example, Deul (1988) presented H I contour maps (20′ resolution) for comparison with 100 μm *IRAS* data for several cirrus clouds. Close examination of his maps reveals that, while the morphology in the H I is closely mimicked by the dust, the H I ridge lines rarely coincide perfectly with the dust structures. The offsets range from 20′ to 40′, comparable to those seen in Eridanus. Similarly, the results of de Vries et al. (1987) on the correlation between dust and gas in another high-latitude region showed a good correspondence between maps of integrated H I emission and *IRAS* data, but, upon close examination, differences can be found between the H I and 100 μm contours, suggesting that some dust has no H I counterpart and vice versa. Unfortunately they did not publish the bandwidth of their 21 cm observation, nor did they present individual H I velocity maps, which would allow closer comparison along the lines we have adopted in this study. The Ophiuchus region shows another example of offsets (estimated to be of order 1°) between H I and IR filaments (de Geus & Burton 1991), again associated with a large shell.

Historically, it has long been known that there is a zero offset in the high-latitude correlation between H I column density and galaxy counts on scales of several degrees, in the sense that a nonzero amount of H I must exist before the extinction begins to increase with N_{HI} (Burstein & Heiles 1978). It has been surmised that this was just an instrumental effect, caused by radio telescope response to stray radiation, but we have pointed out in § 2.1 that all of our signal contours are at least 10 times greater than the stray radiation uncertainties of our data. The zero offset in the correlation of Burstein & Heiles (1978) corresponds to $N_{HI} \approx 10^{20}$ cm^{-2}, which is comparable to the column densities in filament A1, but is an order of magnitude below the total H I column density of the region (e.g. Fig. 12). We do not believe that our results represent a general breakdown in the correlation between gas and dust at low column densities, because the variations in the dust/gas ratio within our map do not follow N_{HI} and are clearly associated with specific structures.

We are led to suspect that physically important aspects of the relationship between H I and IR cirrus clouds have been overlooked in studies that have focused on low-resolution comparisons of N_{HI} values with IR surface brightness. If H I and dust are related in the way we have found in the present work, then correlation diagrams showing line-of-sight gas and dust contents at high resolution (e.g., Roger, Purton, & Willis 1990) will be expected to lead to a large range of ratios and may have little physical significance.

6. CONCLUSIONS

To our knowledge, this is the first study to claim to have found an interstellar cloud in which there is a clearly visible, statistically significant, and physically real separation between gas and dust, such that the dust/gas mass ratio varies locally by an order of magnitude.

The separation between the gas and dust filaments at the edge of the expanding shell in Eridanus can be described in several ways. The most obvious demonstration is that when H I and IR maps at the same resolution are overlaid (Fig. 9), the two tracers show similar morphological features, but markedly offset from each other. As described in § 2.1 and Table 1, we have made a series of checking observations to make sure that the positions at which we place the filaments are correct. In § 3.1 and Table 2 we measure the separation between the filaments and its uncertainty, proving that the separation is highly significant.

The apparent separation between structures in the H I and IR maps is not an artifact that occurs because the gas has made a transition into another phase. Large-scale maps of Hα emission from this region show that the ionized hydrogen lies in filaments that parallel the H I and IR filaments 3°–4° away (§§ 1 and 2.4, Figs. 1 and 8). There is a small, apparently normal, molecular cirrus cloud MBM 15 that is located in a part of this region where the H I and IR emission appear to wrap around each other, and where the H I velocities suggest that two filaments may have collided (Figs. 2, 10, and 11). Otherwise, our molecular observations place CO upper limits on these filaments that are ≈ 50 times below the cloud peaks, and from the conditions in MBM 15 we infer that the H_2 column densities in the rest of the filaments are at least two orders of magnitude below what is typically seen in high latitude molecular clouds (§ 3.2, Tables 3 and 4, Fig. 12).

Another way of describing the separation between the gas and dust filaments at the edge of the expanding shell in Eridanus is to compare their observed dust/gas ratios with the predicted ratio at high Galactic latitudes. We adopt an expected dust/gas mass ratio in cirrus of $\sim 1 \times 10^{-3}$ from Sodroski et al. (1987). In § 4.2 and Table 5 we show that the primary H I filament in the region, which maintains a narrowly defined velocity over a length of 30°, is deficient in dust by an order of magnitude. The corresponding dust filament has sufficient gas to satisfy the dust/gas ratio at any given point. It is nonetheless odd that at the locations of the dust filament contours, there is no matching structures in atomic or molecular hydrogen column density (e.g., Fig. 13). In this sense, the dust filament as a whole still has an apparent gas deficiency.

Yet another way of describing the separation between the gas and dust filaments at the edge of the expanding shell in Eridanus is to compare their ratios of $I_{100}/N_{\rm H\,I}$ with observations of other regions. This comparison is not as robust as the dust/gas mass ratio, because I_{100} is dominated by the warmest dust along the line of sight. However, $I_{100}/N_{\rm H\,I}$ is often computed in the literature and is found to be $\sim 1.0 \times 10^{-20}$ MJy sr^{-1} cm^2 at high Galactic latitudes, with a factor of 3 variation from region to region. On a point-by-point basis, I_{100} and $N_{\rm H\,I}$ show a very weak correlation for this region as a whole (Fig. 14), or for the peaks of the H I or IR filaments separately; but when I_{100} and $N_{\rm H\,I}$ are compared at corresponding (offset) peaks and valleys in the IR and H I filaments respectively, there is a good correlation and the ratio is 0.55×10^{-20} MJy sr^{-1} cm^2 (§ 4.3). We note that the method of computing $N_{\rm H_2}/W_{\rm CO}$ that was developed by de Vries, Heithausen, & Thaddeus (1987) breaks down when applied to regions like the Eridanus filaments (§ 3.2); their method assumes that I_{100} is proportional to the total gas column density, which is invalid on small scales.

We have considered a variety of hypothetical scenarios which might "explain away" the separation of gas and dust as an illusion. All of the scenarios involve contradictions with the data or are too contrived to seem plausible. We list three:

1. Perhaps the dust temperature increases from the H I to IR filaments, so that the IR emission of the latter appears much stronger. But this hypothesis is physically unreasonable, because no embedded heat sources are seen, and the H I filaments are closer to the hot cavity inside the shell. In fact, the observed IR temperatures are $\sim 5°$ cooler inside the IR filaments (§ 2.3, Fig. 6, Table 5).

2. Perhaps the majority of the dust in the filaments is not registered by *IRAS* because it is very cold. But keeping this dust cold when it is embedded in the diffuse rim of a shell created by an energetic event would require shielding it somehow, perhaps in dense clumps. This leads to the secondary hypothesis that the molecular hydrogen content of the filaments has been underestimated. But our CO upper limits are quite severe (§ 3.2). The only way to hide molecular gas would be if the observed CO is underexcited. This would require the gas density and/or abundance to drop drastically outside of the embedded cloud MBM 15, which is possible but contrived and anyway would not provide the dense clumps needed to hide cold dust.

3. Perhaps the filaments contain unresolved clumps in a variable distribution which, when subjected to beam dilution during observation, produces apparent variations in column density. Although there is a great deal of unresolved and explained small-scale structure in the H I and IR emission of these filaments (§§ 2.1 and 3.3), this possibility is also extremely contrived.

The morphological resemblance of the offset H I and IR filaments, plus the fact that they would produce a normal $I_{100}/N_{\rm H\,I}$ ratio if superposed, suggests that the two filaments were once coincident. The structure and velocities of the filaments, as well as their association with the Eridanus shell, indicate that they were once accelerated by a shock front. In § 5.1 we considered shock and radiation mechanisms that might cause a radial separation of gas and dust, with the dust on the outer rim of the shell, or that might have destroyed dust on the inner edge of the shell. Previous work suggests that the coupling between gas and dust is too efficient for a noticeable offset to be accumulated from relative streaming motions, and models that attribute the dust deficiency in the H I filament to shock destruction have difficulty explaining the apparent normalcy of the adjacent IR filament. Future theoretical work is needed; none of these mechanisms has been completely modeled under conditions relevant to interstellar cirrus at high Galactic latitudes.

The large expanding shell in Eridanus is the "best example visible" in the Galaxy (Heiles 1976) of a phenomenon known as "superbubbles" (Tenorio-Tagle & Bodenheimer 1988). We now know that our Galaxy and others are riddled with hot expanding cavities that are created by the sequential formation and explosion of massive stars. We have adopted a distance of 400 pc to the filaments in this study (§ 4.1). As superbubbles are common in galaxies, the phenomenon which we have dis-

covered in Eridanus may be common. We note in § 5.2 that several recent comparisons of H I and *IRAS* maps by other workers seem to show similar separations when reexamined with an outlook that is open to this possibility. Work in progress to compare high-latitude *IRAS* emission with high-resolution H I maps from telescopes in Penticton (Roger et al. 1990) and Arecibo (by one of us, G. L. V., 1991) find similar results. We suspect that large fluctuations in the local dust/gas ratio may not be so much a product of shock and radiation processing in superbubbles, as a general property of the interstellar medium when viewed at high angular resolution.

The search for and study of additional cases of separation between gas and dust filaments will require favorable viewing geometry, H I surveys at resolutions of 10′ or better, and careful data analysis. We emphasize that accurate infrared opacities for weak emission at high latitudes (e.g., Fig. 7) requires careful background subtraction, and an awareness that uncertainties in the band-to-band calibration of the *IRAS* satellite imply a 20% error bar on the 60 μm/100 μm intensity ratio. An awareness of background levels also applies to the gas observations. For instance, when we compare the predicted and observed dust/gas ratio of the primary filament (§ 4.2), we use only the H I at the filament velocity. By contrast, when we compute the $I_{100}/N_{\rm H\,I}$ ratio (§ 4.3), we follow other authors and use all the H I along the line of sight.

We urge a more careful examination of interstellar structures for further examples of separations between gas and dust components, and new theoretical work to explain the origin of these separations. Further study of the Eridanus filaments is needed to improve their distance estimate and to map their small-scale structure at higher angular resolution.

We are grateful to T. M. Bania for his help in arranging the 21 cm observations at the Bonn 100 m telescope and the CO observations at the AT&T Bell Laboratories 7 m telescope, and to T. Wilson for obtaining the H I data. We thank T. Dame for taking preliminary CO observations with the Harvard-Smithsonian Center for Astrophysics 1.2 m telescope. We are especially grateful to P. A. Henning and F. J. Kerr for taking enough time while observing the region with the NRAO 43 m telescope so as to allow us to determine the positional accuracy of the H I data. Thanks are due to A. Warnock for help in transferring H I contour maps to data files, to S. Stemwedel for help in tracking stellar data through SIMBAD, to J. Ware for her patience and skill in rendering the figures fit for publication, and to E. Dwek and R. Reynolds for helpful discussions. We appreciate the careful review of our manuscript by the referee, Loris Magnani. G. L. V. is particularly grateful for the support of J. T. Schmelz. L. J. R. was supported in part by the Office of Naval Research. F. V. was supported by a Research Associateship from the National Research Council, by NASA ADP grants to proposals 074-89 and 092-89, and by grant LTSA-89-100 from the NASA Long-Term Space Astrophysics Research Program. D. L. was supported by NASA ADP grant R033-88.

REFERENCES

Bazell, D., & Desert, S. X. 1988, ApJ, 33, 353
Bloemen, J. B. G. M., et al. 1986, A&A, 154, 25
Bohlin, R., Savage, B. D., & Drake, J. F. 1978, ApJ, 224, 132
Boulanger, F., & Pérault, M. 1988, ApJ, 330, 964
Brand, P. W. J. L., & Zealey, W. J. 1975, A&A, 38, 363
Burstein, D., & Heiles, C. 1978, ApJ, 225, 40
Colomb, F. R., Pöpel, W. G. L., & Heiles, C. 1980, A&AS, 40, 47
de Geus, E. J., & Burton, W. B. 1991, A&A, 246, 559
de Vries, H. W., Heithausen, A., & Thaddeus, P. 1987, ApJ, 319, 723
Deul, E. 1988, Ph.D. thesis, University of Leiden
Diamond, P. J., Goss, W. M., Romney, J. D. Booth, R. S., Kalberla, P. M. W., & Mebold, U. 1989, ApJ, 347, 302
Draine, B. T., & Anderson, N. 1985, ApJ, 292, 494
Elliott, K. H., & Meaburn, J. 1970, Ap&SS, 7, 252
Frerking, M. A., Langer, W. D., & Wilson, R. W. 1982, ApJ, 262, 590
Gilman, R. C. 1972, ApJ, 178, 423
Heiles, C. 1976, ApJ, 208, L137
Heiles, C., & Habing, H. J. 1974, A&AS, 14, 1
Heiles, C., Reach, W. T., and Koo, B-C. 1988, ApJ, 332, 313
IRAS Catalogs and Atlases, Explanatory Supplement. 1985, ed. C. A. Beichman, G. Neugebauer, H. J. Habing, P. E. Clegg, & T. J. Chester (Washington, DC: US GPO)
Jahoda, K., Lockman, F. J., & McCammon, D. 1990, ApJ, 354, 184
Korhonen, T., & Reiz, A. 1980, A&AS, 64, 487
Lockman, F. J., Jahoda, K., & McCammon, D. 1986, ApJ, 302, 432
Magnani, L., Blitz, L., & Mundy, L. 1985, ApJ, 295, 402
Magnani, L., Blitz, L., & Wouterloot, J. G. A. 1988, ApJ, 326, 909
Magnani, L., Carpenter, J. M., Blitz, L., Kassim, N., & Nath, B. B. 1990, ApJS, 73, 747
Magnani, L., & de Vries, H. W. 1988, A&A, 168, 271
McKee, C. F., Hollenbach, D. J., Seab, C. G., & Tielens, A. G. G. M. 1987, ApJ, 318, 674
Meaburn, J. 1965, Nature, 208, 575
———. 1967, Z. Ap., 65, 93
Mehta, J. S., & Srinivasan, R. 1970, Biometrika, 57, 649
Pound, M. W., Bania, T. M., & Wilson, R. W. 1990, ApJ, 351, 165
Reddish, V. 1971, Nature, 232, 40
Reynolds, R. J., & Ogden, P. M. 1979, ApJ, 229, 942
Reynolds, R. J., Roesler, F. L., & Scherb, F. 1974, ApJ, 192, L53
Roger, R. S., Purton, C. R., & Willis, A. G. 1990, BAAS, 22, 752
Sandage, A. 1976, AJ, 81, 954
Seab, C. G. 1987, in Proc. 1st Wyoming Conf., Interstellar Processes, ed. D. J. Hollenbach & H. A. Thronson, Jr. (Dordrecht: Reidel), 491
Seab, C. G., & Shull, J. M. 1983, ApJ, 275, 652
Sivan, J. P. 1974, A&AS, 16, 163
Sodroski, T. J., Dwek, E., Hauser, M. G., & Kerr, F. J. 1987, ApJ, 322, 101
Spitzer, L., Jr. 1976, Comm. Astroph., 6, 157
Tenorio-Tagle, G., & Bodenheimer, P. 1988, ARA&A, 26, 145
Turner, B. E., Rickard, L. J, & Xu, L.-P. 1989, ApJ, 344, 292
Verschuur, G. L. 1973, AJ, 78, 573 (Paper I)
———. 1974, ApJS, 27, 65
———. 1989, ApJ, 339, 163
———. 1992, in preparation
Verschuur, G. L., Cram, T. R., & Giovanelli, R. 1973, A&A, 12, 203
Verter, F., Magnani, L., & Dwek, E. 1988, BAAS, 20, 1060
Welch, B. L. 1937, Biometrika, 29, 350
Williamson, F. O., Sanders, W. T., Kraushaar, W. L., McCammon, D., Borken, R., and Bunner, A. N. 1974, ApJ, 193, L133